

REF ID: A222 529 FILE COPY

2

AD-A222 529



Defense Nuclear Agency  
Alexandria, VA 22310-3398



DNA-TR-89-137

## Observations of the Plasma Structure "Freezing" Scale at Equatorial Latitudes

R. C. Livingston and J. F. Vickrey  
SRI International  
333 Ravenswood Avenue  
Menlo Park, CA 94025-3434

May 1990

Technical Report

DTIC  
ELECTE  
MAY 17 1990  
S E D

CONTRACT No. DNA 001-86-C-0002

Approved for public release;  
distribution is unlimited.

90 05 16 172

Destroy this report when it is no longer needed. Do not return to sender.

PLEASE NOTIFY THE DEFENSE NUCLEAR AGENCY,  
ATTN: CSTI, 6801 TELEGRAPH ROAD, ALEXANDRIA, VA  
22310-3398, IF YOUR ADDRESS IS INCORRECT, IF YOU  
WISH IT DELETED FROM THE DISTRIBUTION LIST, OR  
IF THE ADDRESSEE IS NO LONGER EMPLOYED BY YOUR  
ORGANIZATION.



## DISTRIBUTION LIST UPDATE

This mailer is provided to enable DNA to maintain current distribution lists for reports. We would appreciate your providing the requested information.

- ☐ Add the individual listed to your distribution list.
- ☐ Delete the cited organization/individual.
- ☐ Change of address.

**NOTE:**  
*Please return the mailing label from the document so that any additions, changes, corrections or deletions can be made more easily.*

NAME: \_\_\_\_\_

ORGANIZATION: \_\_\_\_\_

### OLD ADDRESS

### CURRENT ADDRESS

\_\_\_\_\_  
\_\_\_\_\_  
\_\_\_\_\_

\_\_\_\_\_  
\_\_\_\_\_  
\_\_\_\_\_

TELEPHONE NUMBER: (    ) \_\_\_\_\_

SUBJECT AREA(s) OF INTEREST:

\_\_\_\_\_  
\_\_\_\_\_  
\_\_\_\_\_

\_\_\_\_\_  
\_\_\_\_\_  
\_\_\_\_\_

DNA OR OTHER GOVERNMENT CONTRACT NUMBER: \_\_\_\_\_

CERTIFICATION OF NEED-TO-KNOW BY GOVERNMENT SPONSOR (if other than DNA):

SPONSORING ORGANIZATION: \_\_\_\_\_

CONTRACTING OFFICER OR REPRESENTATIVE: \_\_\_\_\_

SIGNATURE: \_\_\_\_\_

CUT HERE AND RETURN



Director  
Defense Nuclear Agency  
ATTN: TITL  
Washington, DC 20305-1000

Director  
Defense Nuclear Agency  
ATTN: TITL  
Washington, DC 20305-1000

REPORT DOCUMENTATION PAGE			Form Approved OMB No. 0704-0188	
Public reporting burden for this collection of information is estimated to average 1 hour per response including the time for reviewing instructions, searching existing data sources, gathering and maintaining the data needed, and completing and reviewing the collection of information. Send comments regarding this burden estimate or any other aspect of this collection of information, including suggestions for reducing this burden, to Washington Headquarters Services, Directorate for Information Operations and Reports, 1215 Jefferson Davis Highway, Suite 1204, Arlington, VA 22202-4302, and to the Office of Management and Budget, Paperwork Reduction Project (0704-0188), Washington, DC 20503.				
1. AGENCY USE ONLY (Leave blank)	2. REPORT DATE 900501	3. REPORT TYPE AND DATES COVERED Technical 870701 - 881231		
4. TITLE AND SUBTITLE Observations of the Plasma Structure "Freezing" Scale at Equatorial Latitudes		5. FUNDING NUMBERS C - DNA 001-86-C-0002 PE - 62715H PR - RB TA - RX WU - DH200891		
6. AUTHOR(S) R. C. Livingston and J. F. Vickrey		8. PERFORMING ORGANIZATION REPORT NUMBER SRI Project 1700		
7. PERFORMING ORGANIZATION NAME(S) AND ADDRESS(ES) SRI International 333 Ravenswood Avenue Menlo Park, CA 94025-3434		10. SPONSORING/MONITORING AGENCY REPORT NUMBER DNA-TR-89-137		
9. SPONSORING/MONITORING AGENCY NAME(S) AND ADDRESS(ES) Defense Nuclear Agency 6801 Telegraph Road Alexandria, VA 22310-3398 RAAE/Schrock		11. SUPPLEMENTARY NOTES This work was sponsored by the Defense Nuclear Agency under RDT&E RMC Code B3220854693 RB RX 00002 25904D.		
12a. DISTRIBUTION/AVAILABILITY STATEMENT Approved for public release; distribution is unlimited.		12b. DISTRIBUTION CODE		
13. ABSTRACT (Maximum 200 words) In this report, we have made the most comprehensive experimental study of the spectral characteristics of equatorial ionospheric F region structure carried out to date. This investigation has included rf propagation measurements as well as in-situ satellite and rocket observations scanning both vertically and horizontally across the magnetic field. Provided that care is taken to avoid strong scatter effects in the propagation data, all of the techniques provide a similar characterization of the plasma concentration fluctuation spectrum—a two-component power law form. The agreement between the horizontal and vertical scans indicates isotropy of the plasma irregularities in the plane perpendicular to the magnetic field. The "freezing" scale, which we have identified with the "break" or change of slope of the power spectrum, moves to larger scale sizes with increasing altitude. The dependence of this behavior is well matched by the inverse of the ion-neutral collision frequency.				
14. SUBJECT TERMS Irregularities, Power Spectral Density, F Layer		15. NUMBER OF PAGES 50		
		16. PRICE CODE		
17. SECURITY CLASSIFICATION OF REPORT UNCLASSIFIED	18. SECURITY CLASSIFICATION OF THIS PAGE UNCLASSIFIED	19. SECURITY CLASSIFICATION OF ABSTRACT UNCLASSIFIED	20. LIMITATION OF ABSTRACT SAR	

**UNCLASSIFIED**

**SECURITY CLASSIFICATION OF THIS PAGE**

**CLASSIFIED BY:**

N/A since Unclassified

**DECLASSIFY ON:**

N/A since Unclassified

## CONVERSION TABLE

Conversion factors for U.S. customary  
to metric (SI) units of measurement

To Convert From	To	Multiply By
angstrom	meters (m)	1.000 000 X E-10
atmosphere	kilo pascal (kPa)	1.013 25 X E+2
bar	kilo pascal (kPa)	1.000 000 X E+2
barn	meter <sup>2</sup> (m <sup>2</sup> )	1.000 000 X E-28
British Thermal unit (thermochemical)	joule (J)	1.054 350 X E+3
calorie (thermochemical)	joule (J)	4.184 000
cal (thermochemical )/cm <sup>2</sup>	mega joule/m <sup>2</sup> (MJ/m <sup>2</sup> )	4.184 000 X E-2
curie	giga becquerel (GBq)*	3.700 000 X E+1
degree (angle)	radian (rad)	1.745 329 X E-2
degree Fahrenheit	degree kelvin (K)	$T_K = (1^\circ F + 459.67) / 1.8$
electron volt	joule (J)	1.602 19 X E-19
erg	joule (J)	1.000 000 X E-7
erg/second	watt (W)	1.000 000 X E-7
foot	meter (m)	3.048 000 X E-1
foot-pound-force	joule (J)	1.355 818
gallon (U.S. liquid)	meter <sup>3</sup> (m <sup>3</sup> )	3.785 412 X E-3
inch	meter (m)	2.540 000 X E-2
jerk	joule (J)	1.000 000 X E+9
joule-kilogram (J/Kg) (radiation dose absorbed)	Gray (Gy)**	1.000 000
kilotons	terajoules	4.183
kip (1000 lbf)	newton (N)	4.448 222 X E+3
kip inch <sup>2</sup> (ksi)	kilo pascal (kPa)	6.894 757 X E+3
ktap	newton-second/m <sup>2</sup> (N-s/m <sup>2</sup> )	1.000 000 X E+2
micron	meter (m)	1.000 000 X E-6
mil	meter (m)	2.540 000 X E-5
mile (international)	meter (m)	1.609 344 X E+3
ounce	kilogram (kg)	2.834 952 X E-2
pound-force (lbf avoirdupois)	newton (N)	4.448 222
pound-force Inch	newton-meter (N.m)	1.129 848 X E-1
pound-force/inch	newton/meter (N/m)	1.751 268 X E+2
pound-force/foot <sup>2</sup>	kilo pascal (kPa)	4.788 026 X E-2
pound-force/inch <sup>2</sup> (PSI)	kilo pascal (kPa)	6.894 757
pound-mass (lbm avoirdupois)	kilogram (kg)	4.535 924 X E-1
pound-mass-foot <sup>2</sup> (moment of inertia)	kilogram-meter <sup>2</sup> (kg.m <sup>2</sup> )	4.214 011 X E-2
pound-mass/foot <sup>3</sup>	kilogram/meter <sup>3</sup> (kg/m <sup>3</sup> )	1.601 846 X E+1
rad (radiation dose absorbed)	Gray (Gy)**	1.000 000 X E-2
roentgen	coulomb/kilogram (C/kg)	2.579 760 X E-4
shake	second (s)	1.000 000 X E-8
slug	kilogram (kg)	1.459 390 X E+1
torr (mm Hg, 0°C)	kilo pascal (kPa)	1.333 22 X E-1

\*The becquerel (Bq) is the SI unit of radioactivity; Bp = 1 event/s.

\*\*The Gray (Gy) is the SI unit of absorbed radiation.

# TABLE OF CONTENTS

Section	Page
CONVERSION TABLE .....	iii
FIGURES .....	v
1 INTRODUCTION .....	1
2 PHASE SCINTILLATION DATA: TWO-DIMENSIONAL SPECTRA	3
3 AE-E DATA: HORIZONTAL, ONE-DIMENSIONAL SCANS .....	13
4 PLUMEX DATA: VERTICAL, ONE-DIMENSIONAL SCANS .....	24
5 THE ALTITUDE DEPENDENCE OF THE FREEZING SCALE ...	35
6 CONCLUSIONS .....	37
7 LIST OF REFERENCES .....	39

Accession For	
NTIS GRA&I	<input checked="" type="checkbox"/>
DTIC TAB	<input type="checkbox"/>
Unannounced	<input type="checkbox"/>
Justification	
By	
Distribution/	
Availability Codes	
Dist	Avail and/or Special
A-1	





## FIGURES

Figures		Page
1	Intensity and Phase Spectra for 413 and 1239 MHz from Ancon Wideband Pass, Day 63, 1977, Showing Fresnel Effects. The relative Fresnel scale locations are noted with arrows .....	5
2	Distributions of Single Power-Law Spectral Indices for 413 and 1239 MHz in Weak Scatter at Kwajalein and Ancon .....	8
3	Distributions of the $P_n$ and $P_h$ Phase Spectral Indices for 413 and 1239 MHz, Weak Scatter Conditions at Kwajalein .....	9
4	Distributions of the $P_n$ and $P_h$ Phase Spectral Indices for 413 and 1239 MHz, Weak Scatter Conditions at Ancon .....	10
5	Distributions of Break Frequency for 413 and 1239 MHz Weak Scatter Measured at Kwajalein and Ancon .....	12
6	AE-E Satellite in situ Plasma Density Observations. Intervals of high resolution RPA data are indicated in the top panel and detailed below .....	14
7	Background Conditions Measured by the AE-E Satellite in Terms of Mean Plasma Density and its Fluctuations .....	16
8	Typical Power Spectra of Plasma Density Fluctuations Measured by the AE-E Satellite .....	17
9	Distributions of Spectral Indices for Single Power-Law and Two-Component Spectral Forms .....	19
10	The Distributions of Spectral Break Wavelength Measured by the AE-E Satellite at Two Different Altitudes .....	21
11	Collision Frequency Profiles Estimated on the Basis of the Measured F10.7 cm Flux and the Jacchia Neutral Atmosphere Model .....	23
12	Geometry of the PLUMEX I Experiment, Showing the Rocket Trajectory and Magnetic Field. Altitudes of the field line intersections with the trajectory and the magnetic equator are as indicated .....	25
13	Plasma Density Profile Measured by the PLUMEX Rocket on the Upleg and Downleg Respectively .....	26
14	Macroscale Plasma Density Features Measured by the PLUMEX Rocket .....	28
15	Plasma Irregularity Structure Measured by PLUMEX .....	29

## FIGURES (Concluded)

Figures		Page
16	A 20 km Altitude Segment of the PLUMEX I Upleg Electron Density Profile and its Spectral Form. Shown are the spectra from three overlapped 10-km spectra (dotted), the average spectral shape (dashed), and the least squares fit to the average shape .....	31
17	Plasma Irregularity Structure Measured by PLUMEX for Altitudes from 330 to 400 km .....	32
18	Altitude profile of bread scales measured by PLUMEX .....	34
19	Scatter Plot of Gradient Scale versus $\sigma N/N$ measured by PLUMEX .....	36

# SECTION 1

## INTRODUCTION

It has been long recognized that a number of ionospheric processes belong to the same class of interchange instabilities as those that impact nuclear phenomenology. These include the Rayleigh-Taylor instability that operates at the magnetic equator, the mid-latitude  $\vec{E} \times \vec{B}$  instability that is driven by neutral winds, and the high-latitude  $\vec{E} \times \vec{B}$  instability that is driven by magnetospheric electric fields. Large barium clouds released into the ionosphere also are unstable to these processes, and a number of experiments have been performed in space to study them. The local linear theory for these instabilities has been worked out by many investigators (see review by *Fejer and Kelley*, 1980, and references therein).

The concept of "freezing" associated with plasma irregularities has become a focus for the DNA community. Evidence of freezing—that is, the appearance and persistence of F-region plasma irregularities at a preferred scale size—was first noted in photographs of striations produced by the CHECKMATE nuclear detonation [*W. G. Chesnut*, personal communication]. Since then, this phenomenon has been observed in various plasmas at F-region altitudes, notably barium ion clouds, and the nighttime equatorial and polar ionospheres. Freezing characteristics, and the processes that produce them, are of interest because they appear to be intimately associated with the convective interchange instabilities and are expected to be prominent in the nuclear environment. Despite their acknowledged existence, very little is known experimentally about the freezing characteristics. The freezing scale has been observed to have a nominal value of several

hundred meters and was, at first, thought to vary little, regardless of plasma conditions. This nominal freezing scale has been determined from optical measurements of CHECKMATE, of barium ion-cloud striations, and, as will be presented in detail below, from spectral analysis of in situ plasma density fluctuations and phase scintillation data.

The need for further experimental characterization of the freezing process is crucial because relatively untested theories for its explanation are being implemented in system codes (e.g., SCENARIO, MICE, and MELT). Moreover, it is not obvious that a single mechanism dominates over all others, or whether two or more processes contribute to the formation of the freezing scale. It is, therefore, particularly important to experimentally test candidate theories. To do so, we have examined changes in the freezing scale under varying plasma conditions; we examined different strengths of instability driver, looked at contiguous, but oppositely directed plasma density gradients, and measured changes in freezing scale as a function of altitude (collisionality).

Implicit in the following analysis is the assumption that the freezing scale (originally coined to describe photographic data) is uniquely associated with the break point between slope regimes of a two-component power-law spectrum of plasma density fluctuations. The means we have used to determine the freezing break is to observe the measured spectrum of plasma density fluctuations (or of radio waves passing through those fluctuations). Our analysis uses three different data sets collected in

the naturally disturbed equatorial ionosphere. These are: (1) RF phase scintillation measurements, (2) high-resolution satellite in situ measurements scanning the structure horizontally, and (3) in situ PLUMEX rocket observations scanning the structure vertically. This combination of techniques provides insight into the integrated plasma effects that impact systems, the altitude (collisionality) dependence of the freezing process, and any spectral anisotropy associated with freezing.

In the next section, we examine these

spectral forms using weak scatter phase scintillation data. In Section 3 we compare these results to spectra from a number of orbits of the AE-E satellite. This analysis verifies that the propagation-derived estimates of horizontally sampled spectral form agree with in situ observations. This is followed, in Section 4, by a detailed analysis of the height variations of spectral shape sampled vertically by the DNA PLUMEX rocket, and, in Section 5, by a discussion of the altitude dependence of the freezing scale. We summarize in Section 6.

## SECTION 2

### PHASE SCINTILLATION DATA: TWO-DIMENSIONAL SPECTRA

The DNA Wideband satellite (*Fremouw et al.*, 1978) operated from spring 1976 until late summer 1979. During those years, hundreds of passes of equatorial phase scintillation were obtained at Ancon, Peru, in the Atlantic sector and Kwajalein, Marshall Islands, in the Pacific. At the time of the first Wideband analyses, there had been no systematic study of ionospheric irregularity spectral shape. The Wideband experiment (and, in particular, the phase scintillation measurements) provided information for the first morphological studies of equatorial irregularity structure. As a result, much of the application phenomenology modeling of irregularity spectral shape has been based on these data.

Rino (1979) presents scintillation statistics of a large accumulation of the Wideband equatorial data. Given a homogeneous and weakly disturbed medium with one-dimensional power-law index  $p_1$ , phase screen theory predicts that the phase spectrum of a propagated signal passing through the medium will have index  $p_1+1$ . Because that is an integrated measure of structure along the raypath, the propagation data are not the unambiguous measure of irregularity structure that in situ data are; in practice, diffraction and other propagation effects, and superposed structured regions, can distort a phase spectrum. Nevertheless, in collection, the average phase spectral form can be measured and related to that of the irregularities. Furthermore, the phase scintillation data have direct relevance to the prediction of RF communication and surveillance system performance, which is much of the original motivation for the experimental work.

At the time of the analysis of the data presented by Rino (1979), the generally two-component nature of irregularity spectra had not yet been recognized, and single power-law fits were made to the spectra over an approximate spatial wavelength range of 300 to 3000 m (temporal frequency range 0.1 to 10 Hz). As shown by Rino (1979), the average weak-scatter ( $0.2 < S_4 < 0.5$ ) power-law phase spectral index for the equatorial data was between 2.6 and 2.9, corresponding to a one-dimensional in situ index between 1.6 and 1.9. As pointed out by *Livingston and Dabbs* (1986), when the same data are analyzed using more appropriate spectral analysis techniques than those used in the original analysis (i.e., the temporal data are windowed), the spectral indices are somewhat steeper: 2.9 at Kwajalein and 3.1 at Ancon.

In order to look more carefully at the data in terms of a freezing break and multicomponent spectral form, a selected portion of the Wideband equatorial data were reprocessed. Some results of that analysis, as applied to a characterization of the phase spectrum under both weak and strong scattering conditions, are discussed by *Livingston and Dabbs* (1986). A major concern when using phase spectra to imply irregularity structure is that the particular manifestations of diffraction on the phase spectrum are unknown. By diffraction, we mean any departure from the nominal linear dependence of signal phase on carrier frequency. Unless the diffraction effects can be specifically identified, any conclusions regarding phase spectral shape should be based on weak scatter data only. Under those conditions, phase screen

theory predicts that the phase spectrum is an integrated mapping of the in situ structure, as noted above. Our purpose is to obtain representative values of the phase spectral slopes and break frequency, from which the one-dimensional in situ irregularity spectral form can be implied.

A convenient range of disturbance level to work with which satisfies the weak scatter criterion, is an intensity scintillation level of  $0.2 < S_4 < 0.5$ . The lower limit is necessary to avoid bias of the results caused by noise contamination. The upper limit follows from analysis presented below that shows that above this level of  $S_4$ , phase errors begin to rapidly increase and the phase spectral shape begins to be distorted. There is an enormous dynamic range of equatorial irregularity strength; depending upon the strength, the scintillation data that fall into this weak scatter disturbance range may occur on any of the three Wideband carrier frequencies (137, 413, or 1239 MHz).

Limiting the analysis to weak scatter levels is not without its complications. In particular, Fresnel null structure is superimposed on most of the weak scatter phase spectra we observe. Figure 1 shows an example sequence of simultaneous 413-MHz and 1239-MHz intensity and phase spectra showing Fresnel effects.

(Note that these 1239-MHz spectra are not included in our weak scatter results because their  $S_4$  levels were less than 0.2.) The arrows indicate the expected frequency of occurrence of the first Fresnel intensity peak and phase null, for the given pass geometry, an assumed irregularity anisotropy of 50:1 and a layer height of 350 km. The nulls are conspicuous, even in these spectra that have been smoothed for display, and persist even beyond the weak

scatter limit. To avoid Fresnel null biases when extracting the spectral slopes, two linear least-square fits are obtained over temporal frequency ranges near the low- and high-frequency ends of the phase spectrum. Taking into consideration the average Fresnel null frequencies at 413 and 1239 MHz (*Livingston and Dabbs, 1986*), convenient fit ranges are 0.10 to 0.56 Hz (-1.00 to -0.25 log Hz, approximately 4500 to 800 m spatial scale), and 1.8 to 10.0 Hz (0.25 to 1.00 Hz, approximately 250 to 45 m spatial scale). The means of obtaining the slopes over these fit ranges, and the spectral analysis, per se, are described by *Livingston and Dabbs (1986)*.

We chose 24 Wideband orbits from Ancon and 19 from Kwajalein for the analysis. All were selected because they show consistent scintillation throughout most of each pass—that is, at a variety of propagation geometries. The Ancon data are from the period February through April 1977; the Kwajalein data are from July through September 1977. There is a distinct shift in the season during which the irregularities maximize in the Atlantic and Pacific sectors (*Tsunoda, 1985*). The reprocessed data are taken from the peak scintillation seasons at each longitude.

The measured spectra have been categorized into three shape types: (1) single power law, (2) two-component power law with a shallow long wavelength regime slope ( $p_a$ ) breaking to a more steeply sloped dissipation regime slope ( $p_b$ ), and (3) the reverse two-component form. This categorization is somewhat arbitrary, and is not meant to imply that the different forms are manifestations of different irregularity generation mechanisms. Instead, there is a continuum of forms that encompass these three types.

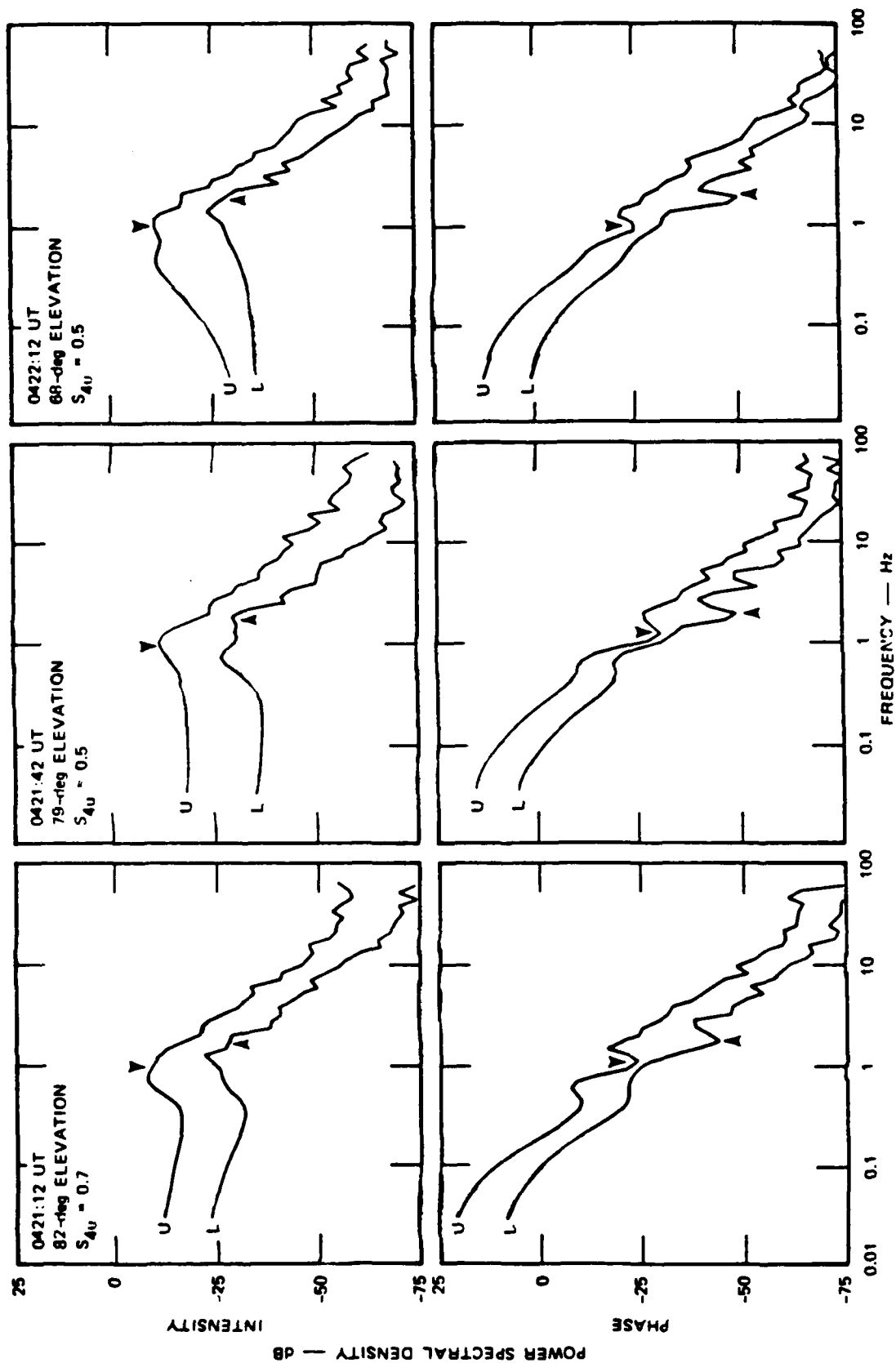


Figure 1. Intensity and Phase Spectra for 413 and 1239 MHz from Ancon Wideband Pass, Day 63, 1977, Showing Fresnel Effects. The relative Fresnel scale locations are noted with arrows.

When the two measured slopes are within 20% of one another, they are considered single-component power-law spectra. As Table 1 shows, these comprise approximately 30% of the overall spectral population. Spectra of the third category are those for which  $p_a$  is significantly steeper than  $p_b$ . Although this form accounts for nearly 30% of the spectra at Ancon (and nearly 40% at Kwajalein), we will not consider those spectra here. Our justification is that this spectral form is almost never observed in situ at the equator (as will be shown in Section 3). Most likely, the phase spectra of this type are a result of integration through more than just a homogeneous F layer; simulations have shown that superposition of the phase energy from a high-density E region can readily produce such a spectral form.

The average measured Wideband phase spectral slope data are summarized in Table 1, as a function of receiving site and carrier frequency. The slope distributions from which these averages are derived are shown in Figure 2 (single power-law population), Figure 3 (Ancon two-component population), and Figure 4 (Kwajalein two-component population). In order to simplify comparison with the in situ data, the average indices in Table 1 are given in terms of the equivalent one-dimensional form, as would be measured by a satellite or rocket probe. As previously mentioned, a difference of unity between the slopes of phase and in situ spectra is predicted by phase screen propagation theory at these weak scatter levels. The widths of the distributions in Figures 2 through 4 are also summarized in Table 1 in terms of their 10th and 90th percentile one-dimensional equivalents.

There are several important points to be made from Table 1, in addition to the

measured spectral index values. The first is the similarity of spectral slopes (both one and two component) at the different carrier frequencies. Propagation theory predicts that although the energy in the phase spectra will vary from carrier to carrier, the spectral shape will not. The agreement between the slope values measured at different carriers (e.g., Ancon 137/413/1239 MHz) assures that the fits are being made without the influence of Fresnel null effects. The agreement between spectral shapes at different carriers also says that the spectral form is not dependent upon disturbance level. The irregularity structure producing the weak scatter scintillation at 1239 MHz is several times stronger than that causing the same disturbance at 413 MHz, yet their spectral forms are nearly identical.

It is also instructive to look at the slope values in Table 1 relative to previously published results. We have already mentioned the Rino (1979) results and the limitations of their applicability. Figure 12 of *Livingston and Dabbs* (1986) summarizes the average weak scatter spectral slope of the Ancon and Kwajalein data, assuming that all of the spectra are single power law in form. For Ancon, their overall power-law slope is close to that of the single power-law populations in Table 1 at the three carriers. Furthermore, the average of the Ancon two-component indices in Table 1 (which is a good approximation to what would be obtained from a single power-law fit over the same spectra) is also close to the same value. However, for the Kwajalein data, *Livingston and Dabbs* (1986) reported a significantly lower average spectral slope (about 1.9 in situ) from single power-law fits over all of the spectra, relative to Ancon. Until recently, this has been generally considered to be a result of different (but unidentified) structuring



Table 1. Summary of phase spectral characteristics.

Wideband 1977-1978

Kwajalein (413 MHz, 254 samples)					
Power Law Type	Population (%)	Slope	Slope Range 10th-90th Percentile	Break Scale (m)	Break Range 10th-90th Percentile
one	30	2.2	1.5 to 2.8	— —	
two	33	1.3	0.6 to 2.0	530	220 to 1300
$P_a < P_b$		3.0	2.0 to 4.0		
two	37	2.7	1.9 to 3.4		
$P_a > P_b$		0.9	0.2 to 1.6	— —	

Kwajalein (1239 MHz, 76 samples)					
Power Law Type	Population (%)	Slope	Slope Range 10th-90th Percentile	Break Scale (m)	Break Range 10th-90th Percentile
one	25	2.0	1.5 to 2.6	— —	
two	34	1.4	0.7 to 2.0	570	200 to 1700
$P_a < P_b$		3.2	2.3 to 4.1		
two	41	2.5	1.8 to 3.2		
$P_a > P_b$		1.0	0.3 to 1.7	— —	

Ancon (137 MHz, 110 samples)					
Power Law Type	Population (%)	Slope	Slope Range 10th-90th Percentile	Break Scale (m)	Break Range 10th-90th Percentile
one	32	2.3	1.8 to 2.9	— —	
two	38	1.3	0.5 to 2.2	420	170 to 1100
$P_a < P_b$		3.1	2.1 to 4.2		
two	30	2.5	1.6 to 3.3		
$P_a > P_b$		0.9	0.2 to 1.6	— —	

Ancon (413 MHz, 317 samples)					
Power Law Type	Population (%)	Slope	Slope Range 10th-90th Percentile	Break Scale (m)	Break Range 10th-90th Percentile
one	26	2.1	1.5 to 2.7	— —	
two	46	1.2	0.3 to 3.4	530	200 to 1400
$P_a < P_b$		3.2	2.1 to 4.2		
two	28	2.6	1.8 to 3.4		
$P_a > P_b$		1.1	0.4 to 1.8	— —	

Ancon (1239 MHz, 103 samples)					
Power Law Type	Population (%)	Slope	Slope Range 10th-90th Percentile	Break Scale (m)	Break Range 10th-90th Percentile
one	19	2.0	1.2 to 2.8	— —	
two	62	1.1	0.3 to 2.0	480	200 to 1140
$P_a < P_b$		3.3	2.2 to 4.3		
two	18	2.7	2.0 to 3.5		
$P_a > P_b$		0.7	- 0.4 to 1.9	— —	

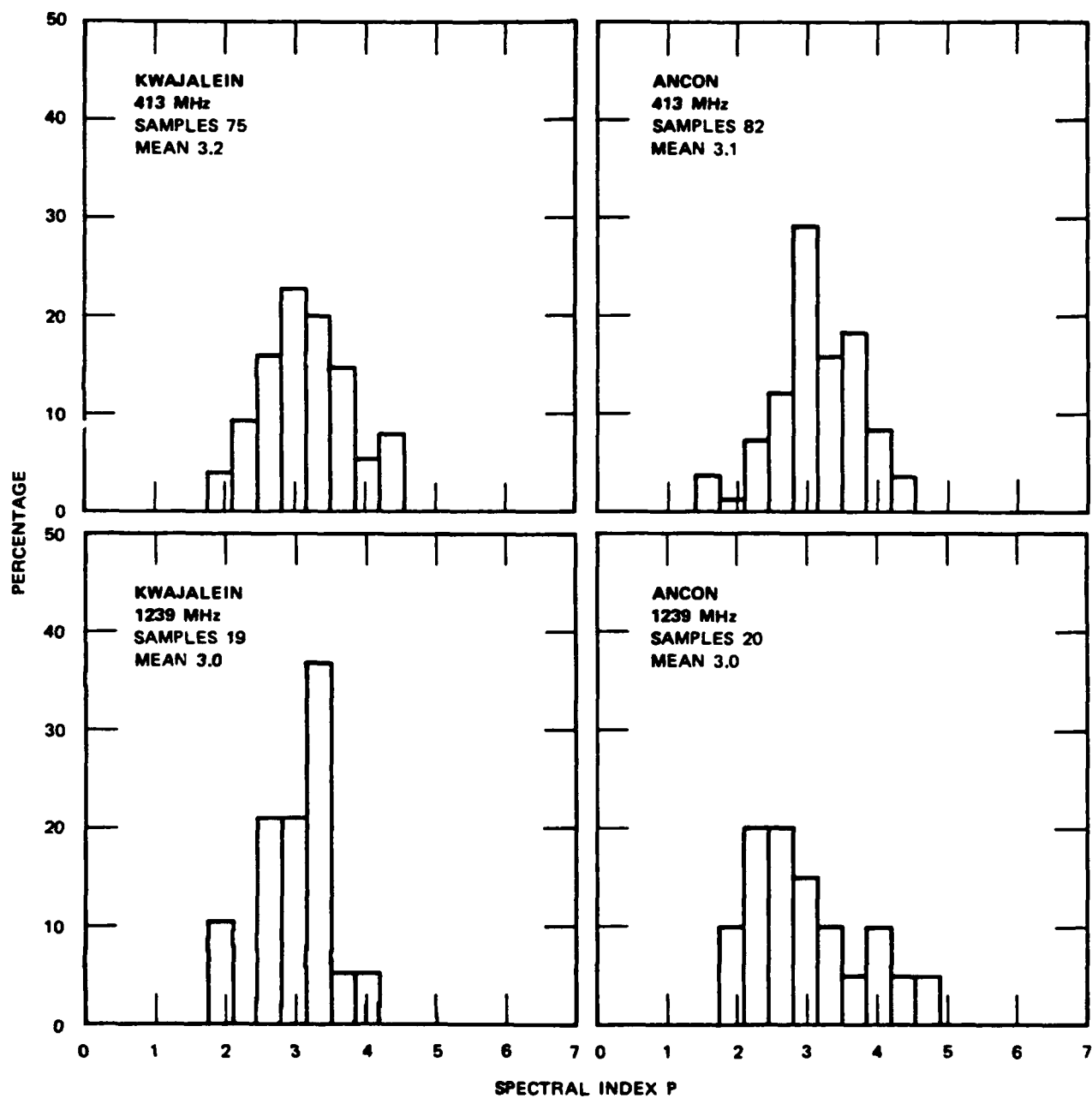


Figure 2. Distributions of Single Power-Law Spectral Indices for 413 and 1239 MHz in Weak Scatter at Kwajalein and Ancon.

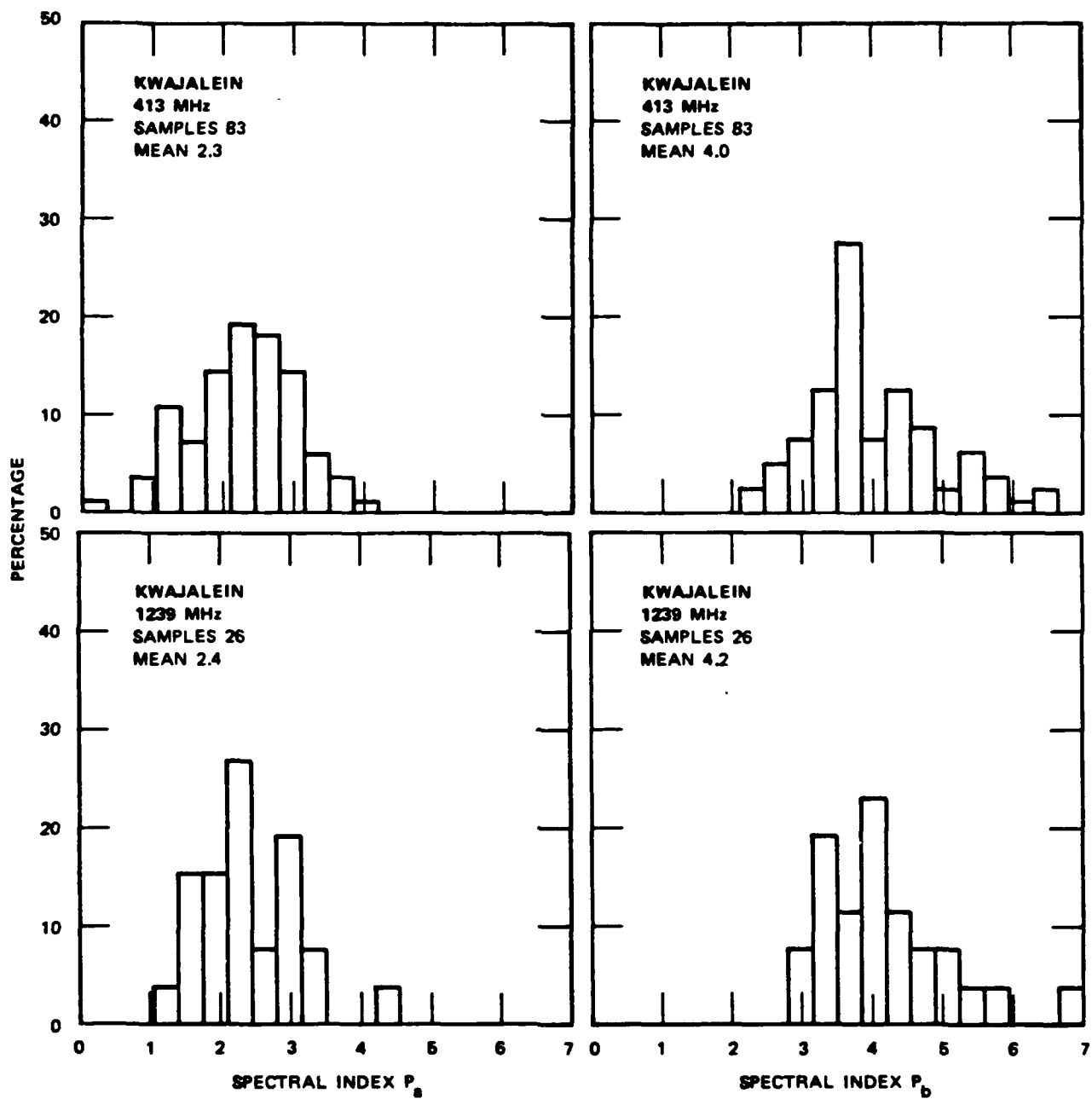


Figure 3. Distributions of the  $P_a$  and  $P_b$  Phase Spectral Indices for 413 and 1239 MHz, Weak Scatter Conditions at Kwajalein.

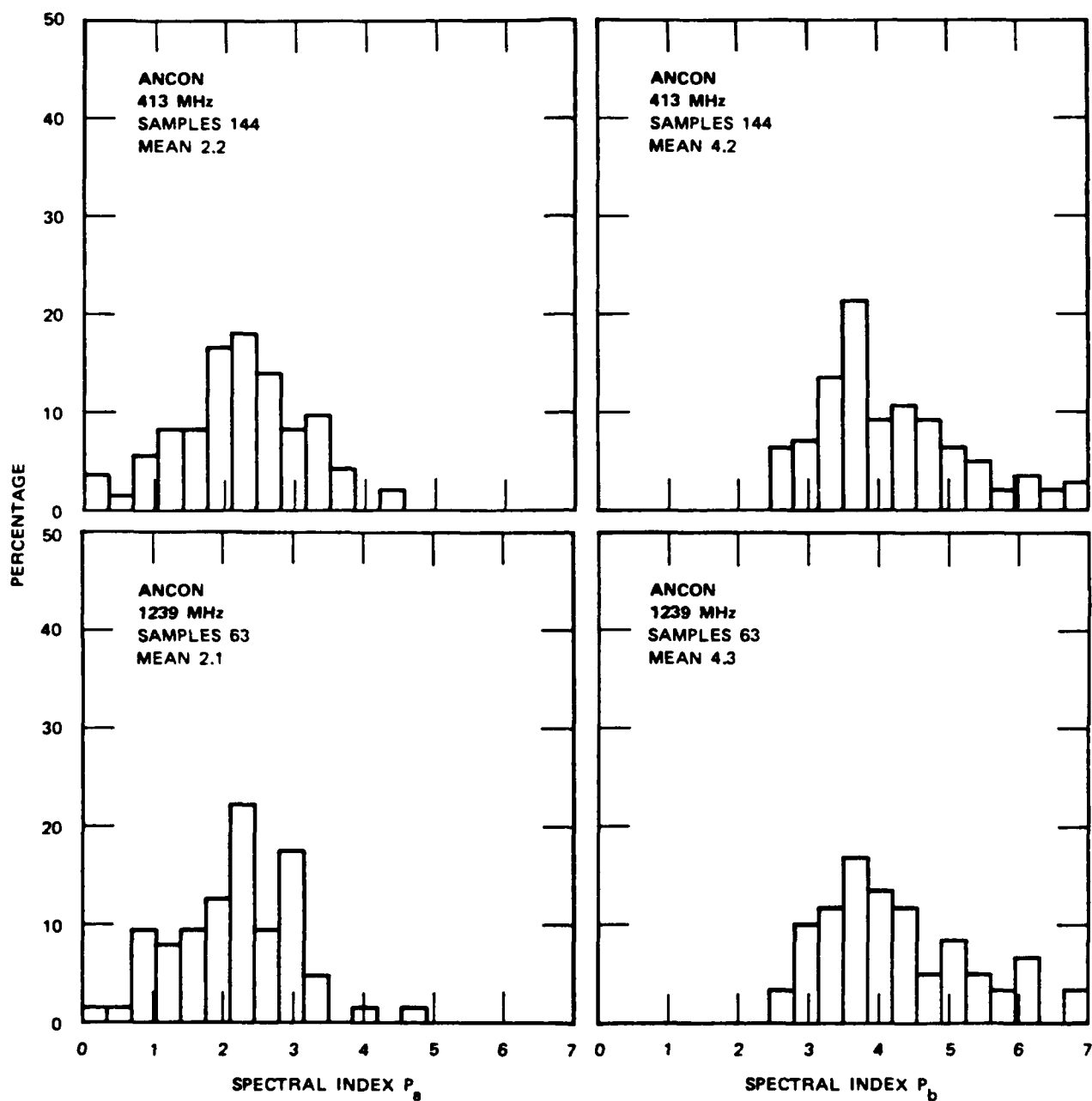


Figure 4. Distributions of the  $P_a$  and  $P_b$  Phase Spectral Indices for 413 and 1239 MHz. Weak Scatter Conditions at Ancon.

processes at the two longitudes. However, Table 1 shows that the Kwajalein single-component and "normal" two-component slopes are very similar to those at Ancon. We conclude that the longitude differences reported in *Livingston and Dabbs* (1986) arise from the inclusion of the "reverse" two-component form spectra in their analysis population. The significantly higher population of these spectra at Kwajalein exaggerates the spectral shallowing there, relative to Ancon.

*Livingston et al.* (1981), also made a study of the spectral shape of a limited segment of Kwajalein Wideband data over a wide range of scatter levels. A conclusion of that report was that the irregularity spectral slope shallowed with increasing irregularity strength. It is now understood that phase spectra shallow during strong scatter conditions because of diffraction (*Livingston and Dabbs*, 1986). We note that the weak scatter portion of the *Livingston et al.* (1981) data, which were fit as single-component power law spectra, exhibit slopes values close to those we observe here.

In addition to the slopes, the spatial scale at which the two-component phase spectrum breaks (the freezing scale) can be determined. In the propagation case, a break in the irregularity spectrum appears in the phase spectrum at a temporal frequency dictated by the line-of-sight scan velocity. This, in turn, depends upon the irregularity altitude, anisotropy, and irregularity motion. The orbital inclination of the Wideband satellite is such that for the premidnight pass data used here, the propagation path scans nearly along the magnetic meridian. For F-region irregularities that are highly extended along the

magnetic field (50:1 or larger anisotropy), the effective scan velocity caused by the satellite motion depends upon propagation geometry, but has an average value of  $\sim 0.45$  km/s. At the local time and latitude of the observations, F-region polarization and tidal electric fields will typically drive the irregularities eastward at a velocity of  $\sim 0.25$  km/s. Thus we can estimate the total effective scan velocity to be in the 0.5- to 0.7-km/s range.

For each two-component spectrum in the population (both normal and reverse forms), the break frequency is determined as the intersection of the  $p_a$  and  $p_b$  linear fit segments. The distribution of the break frequencies is shown in Figure 5 for 413 and 1239 MHz at Ancon and Kwajalein. The distributions are broad, which is primarily a result of the range of sampled propagation geometries and effective scan velocities. If there were a means of accurately applying corrections for the scan velocity so that the data could be sorted in spatial scale, the distributions would be much narrower.

Despite the broadening, the distributions in Figure 5 all peak near the same frequency. Because the temporal frequency at which the translated break occurs is independent of carrier frequency, this lends credence to the interpretation that the origin of the break is in situ. Choosing an overall average break frequency of 1.1 Hz, and a representative scan velocity of 0.60 km/s, our estimate of the irregularity break scale is near 0.55 km. This is in good agreement with the irregularity spectrum break scale observed by satellites and rockets, as will be reviewed in the following sections.

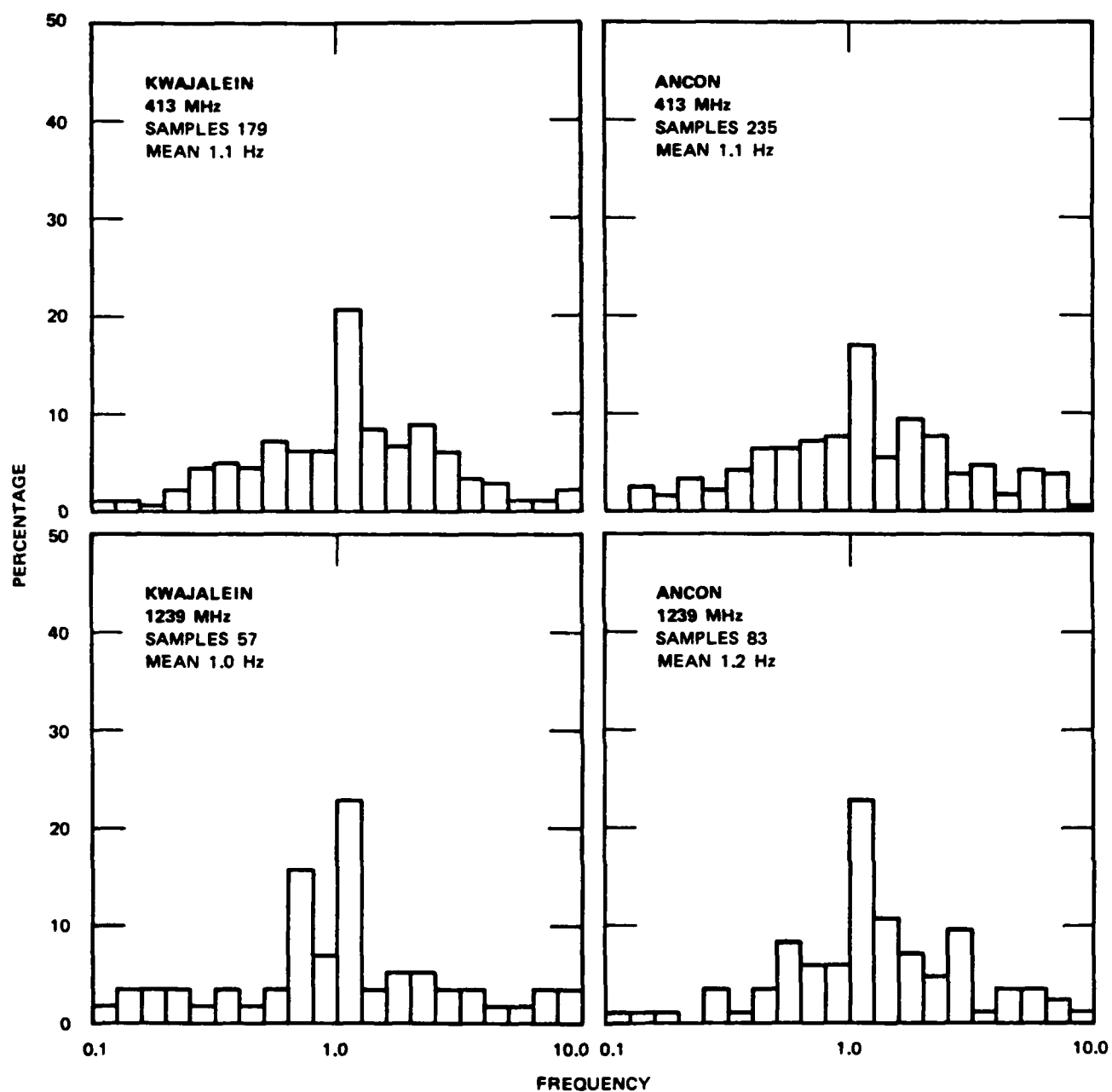


Figure 5. Distributions of Break Frequency for 413 and 1239 MHz Weak Scatter Measured at Kwajalein and Ancon.

## SECTION 3

### AE-E DATA: HORIZONTAL, ONE-DIMENSIONAL SCANS

The Atmospheric Explorer-E (AE-E) satellite mission operated from late 1976 through mid-1979, providing in situ measurements of the equatorial ionosphere. Among the instruments that the spacecraft carried was a retarding potential analyzer (RPA) from which high-resolution measurements of plasma density structure were obtained. A detailed description of the RPA and its associated instrumentation can be found in work by *Hanson and Heelis (1975)*.

Of interest to us here are two periods of time when AE-E was operating at altitudes well within the equatorial F layer. These two periods were in autumn 1978 and winter 1979-1980, when the satellite was at altitudes of 375 and 435 km, respectively. This first period was well onto the upswing of the solar cycle; the latter period was near sunspot maximum. During each period, many orbits of data were obtained. Of these, there were approximately 30 orbits when the RPA instrument was on and the ionosphere that it sampled was significantly structured to merit detailed analysis. Because at low latitudes the F region structures only during the local evening and night hours when F-layer bubbles can occur, the disturbed orbits all correspond to local evening. The previously mentioned seasonal dependence of irregularity occurrence effectively limits the selected 1978 data to Pacific longitudes, and the 1979-1980 data to Atlantic longitudes.

The RPA instrument aboard AE-E did not operate continuously, but rather collected data for three out of each six seconds. Figure 6 shows a series of these samples with respect to the continuous low-

resolution ion density measured by the drift meter. For the orbits of interest, the RPA data spans that exhibited structure (and some degree of stationarity in that structure) were selected for processing. The only structures that were specifically avoided were those obviously dominated by bottom-side spread (BSS) irregularities; these were found primarily in the 375-km data. For each RPA sample, background parameters (e.g., average ion density, density gradient) have been extracted, and the power spectral density of the plasma structure computed.

As an overview of the background conditions, Figure 7a shows the variation of mean ion density with dip latitude; each point corresponds to an RPA record for which spectra have been computed. The figure illustrates that the background densities for the 1978 (375 - km) and 1979-1980 (435-km) measurements are very similar. Both show the same increase in ion density away from the magnetic equator, which is probably a signature of the equatorial anomaly. The similarity of the mean densities is not surprising, because, relative to the F peak, the observation altitudes are nearly the same. Ionosonde measurements collected at Kwajalein during mid-1979 (*Tsunoda and Rino, 1982*) show a typical F-layer bottomside altitude of 350 km at spread-F onset, with a decline to 300 km by midnight. Similar observations made in mid-1981, late in the peak of the solar cycle, show the bottom-side altitudes to be shifted upward by an average of 50 km. We would estimate that in both our 1978 and 1979-1980 data sets,

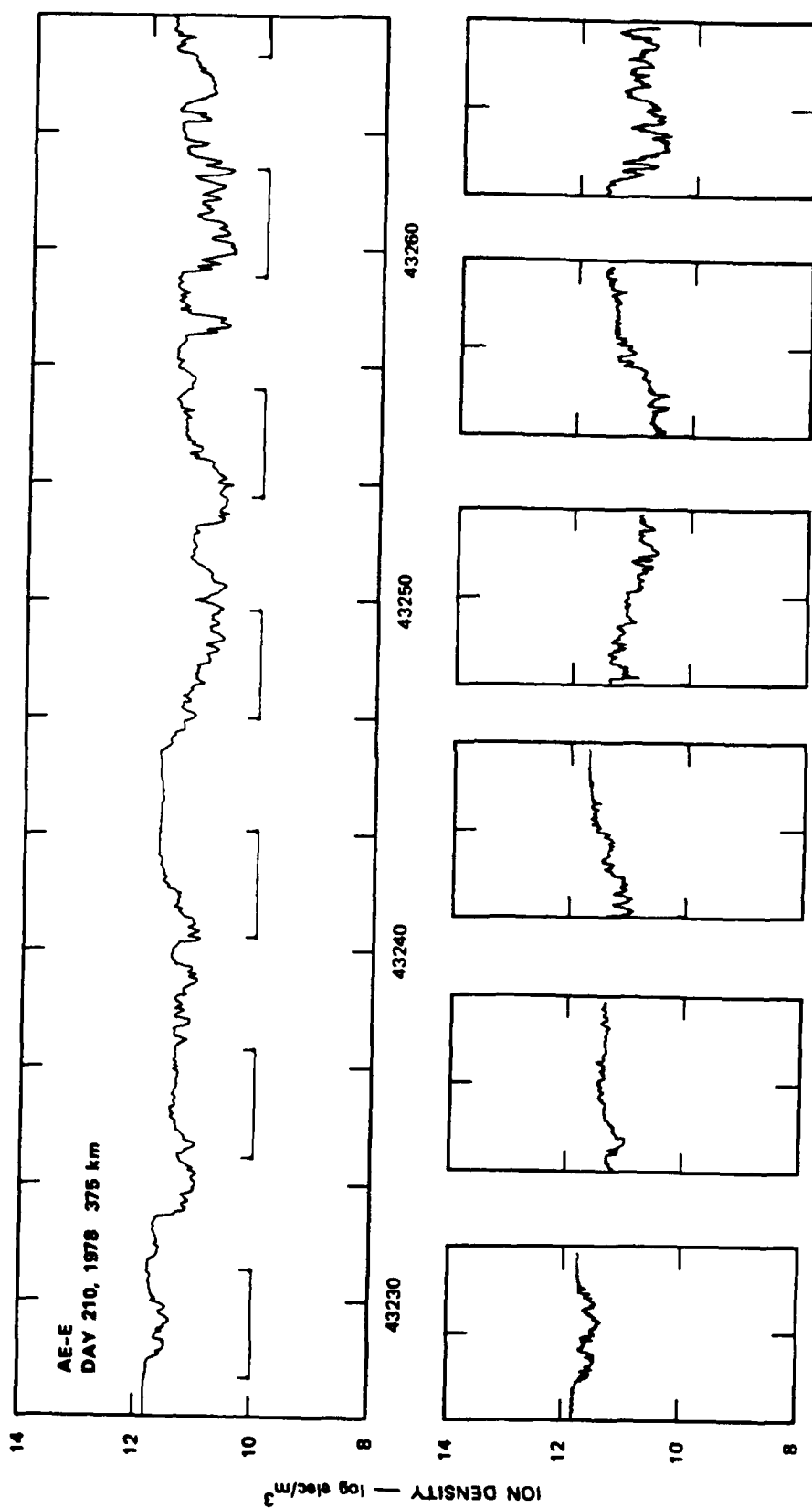


Figure 6. AE-E Satellite in situ Plasma Density Observations. Intervals of high resolution RPA data are indicated in the top panel and detailed below.



the AE-E was very near the average peak of the F layer at local middle evening hours.

The integrated energy in the overall, intermediate scale (200- to 2000-m) ion density structure is shown in Figure 7b. The peak deviations in the anomaly region are similar, but at the dip equator, the average energy is stronger at 375 km. Figure 7c illustrates that both data sets show similar and systematic weakening of the structure with local time as the irregularities, generated by plasma bubble passage, slowly decay.

For our morphological purposes here, the data in Figure 7 show that, in collection, there are no dramatic differences between the two time/altitude periods, in terms of background conditions and level of structuring. This simplifies the comparison of the spectral forms obtained from the two data sets; with no gross differences between the ionospheric conditions (background density or large-scale gradients), the primary structuring processes should be similar.

Figure 8 shows typical power spectra of the ion density irregularities (these are from one orbit in the 1978 series). The spectra are computed in a conventional fashion, using the procedures developed for the HILAT satellite program. The three-second RPA records are edge matched and cosine windowed, before computation of a 600-point FFT. This provides spectral information over a frequency range of 0.5 to 100.0 Hz. For the satellite *scan* velocity of 0.77 km/s, this corresponds to measurement of structure energy at spatial wavelengths between about 80 and 4000 m. The computed spectra are binomially smoothed and log decimated to 50 points, producing the form shown in Figure 8.

One of the difficulties encountered when deriving spectral shape information (slopes and break scales) from multicomponent power-law spectra is that all practical automated fitting algorithms appear to have biases. When the low- and high-frequency portions of a multicomponent spectrum have very different slopes, and the break itself is the dominant spectral feature, accurate fits are derived. However, when the slopes are similar, or the spectrum shows some isolated secondary structure, fits are often obtained that, by eye, do not appear to be optimum. For these AE-E data, it is practical to fit each spectrum interactively. Breaks in the spectra are identified by eye in a computer display, and least-square slope fits to the power-law slope segments between these breaks are determined by the computer. Figure 8 shows that the power-law segments determined this way accurately represent the measured continuum.

The collected spectral form data have been sorted into various spectral types. The populations for each type are determined using measured spectral breaks that are within the freezing break "window" (150- to 2500-m spatial scale); as with the phase spectra in Section 2, adjoining slope segments that are within 20% of one another are considered to be a single power-law segment with no intervening break. Table 2 shows the resulting population of one-, two-, and three-component spectral types. For both time periods, the majority of the spectra are two component in shape, with the expected form: a shallow intermediate scale regime breaking to a more steeply sloped dissipation regime. The reverse form (i.e., more shallowly sloped at short scales) is virtually absent, unlike the phase spectral data. Significant portions, roughly one quarter,

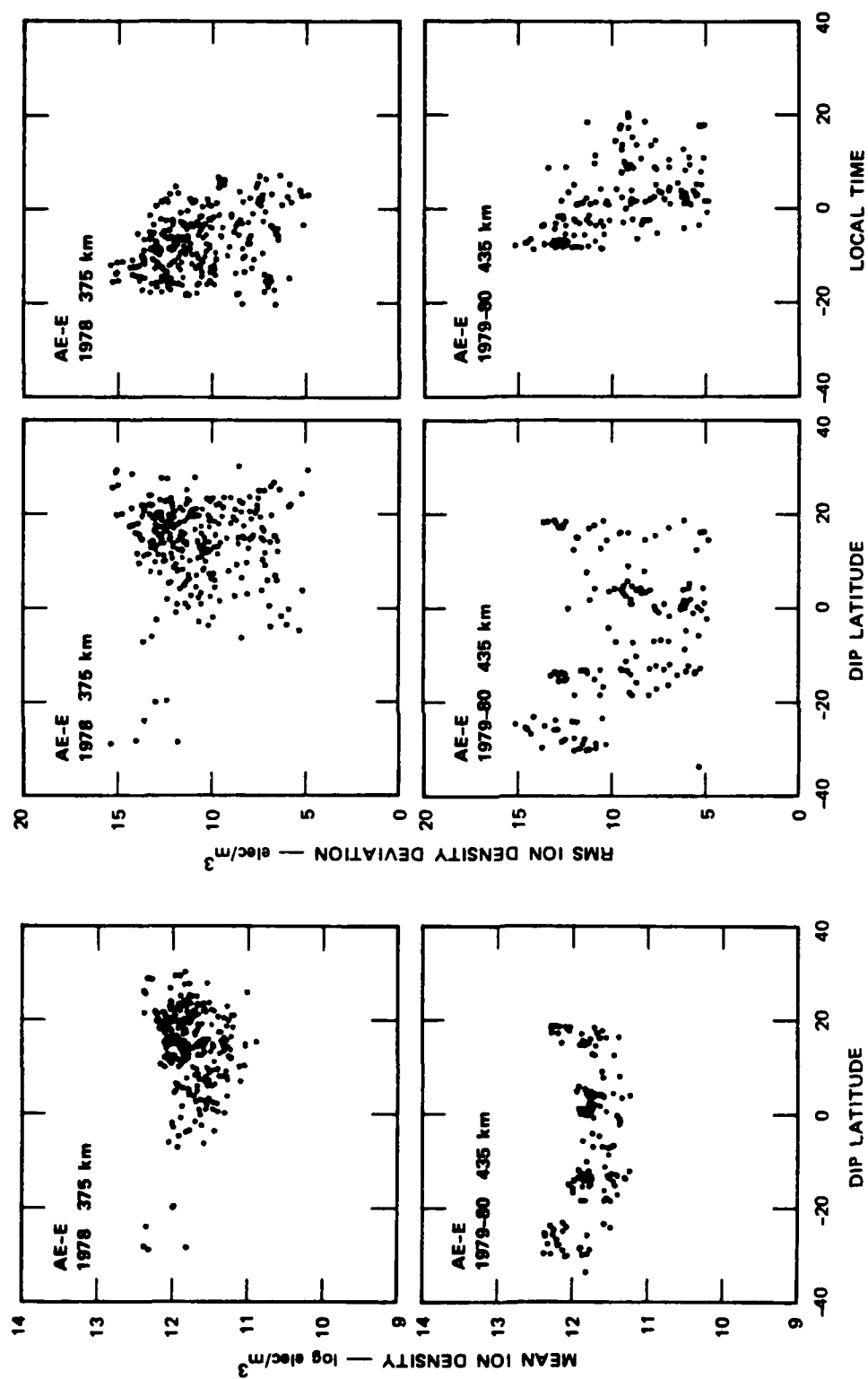


Figure 7. Background Conditions Measured by the AE-E Satellite in Terms of Mean Plasma Density and its Fluctuations.

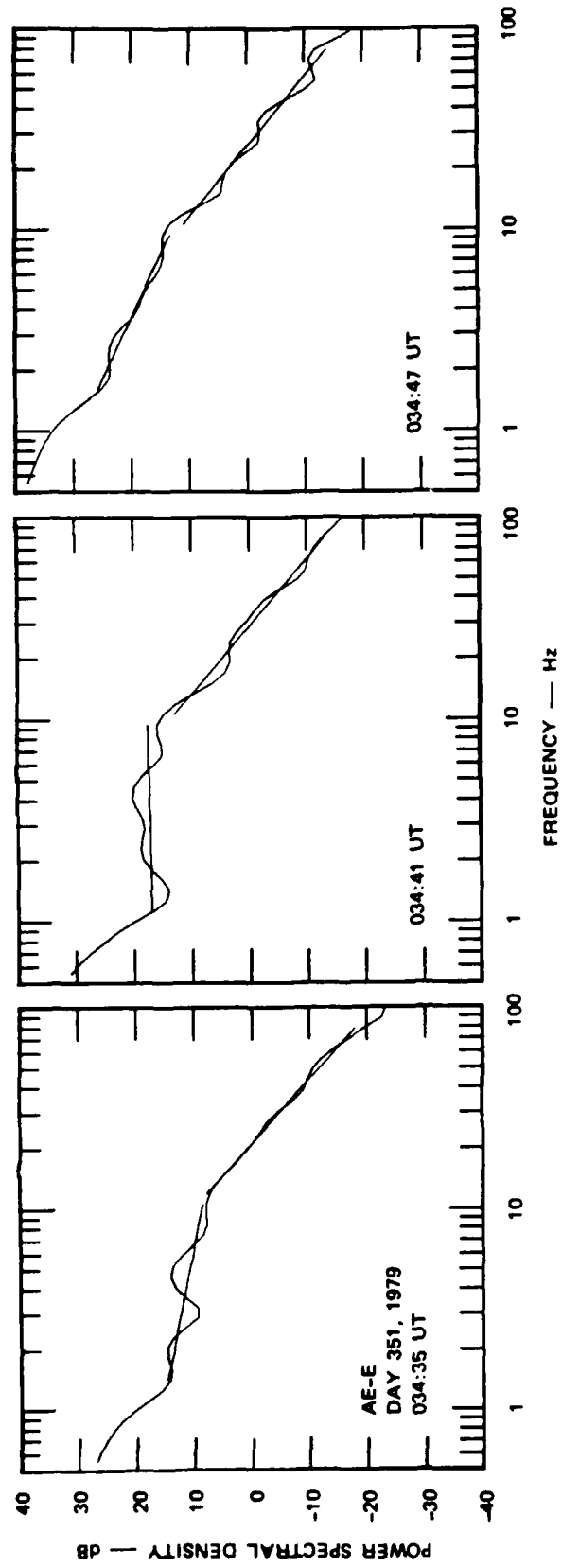


Figure 8. Typical Power Spectra of Plasma Density Fluctuations Measured by the AE-E Satellite.

Table 2. Summary of in situ irregularity spectral characteristics.

AE-E 1978

375 km Altitude, Pacific Sector, 272 samples					
Power Law Type	Population (%)	Slope	Slope Range 10th-90th Percentile	Break Scale (m)	Break Range 10th-90th Percentile
one	23	1.6	1.1 to 2.1	— —	
two	56	0.8	0.1 to 1.5	800	500 to 1300
$P_a < P_b$		2.4	1.9 to 2.9		
two	1	—		— —	
$P_a > P_b$		—			
three	20	0.9	- 0.3 to 2.1	1700	1200 to 2500
		2.0	0.1 to 1.6	350	240 to 550
		2.4	1.4 to 3.4		

AE-E 1979-1980

435 km Altitude, Atlantic Sector, 146 samples					
Power Law Type	Population (%)	Slope	Slope Range 10th-90th Percentile	Break Scale (m)	Break Range 10th-90th Percentile
one	29	1.9	1.3 to 2.5	— —	
two	67	0.9	0.1 to 1.6	720	480 to 1100
$P_a < P_b$		3.0	2.5 to 3.5		
two	1	—		— —	
$P_a > P_b$		—			
three	4	—		— —	
		—		— —	
		—		— —	

of both the 1978 and 1979-1980 populations are best fit by a single power-law segment. The biggest difference between the distributions measured at the two altitudes is the relatively high percentage of three-component spectra in the 1979-1980 data.

Figure 9 shows the distributions of the measured spectral slopes for the single power-law and two-component AE-E spectral forms. These are summarized in Table 2 in terms of the slope mean and 10th/90th percentile range. Although most of the discussion that follows is concerned with

the dominant, two-component spectra, it is worthwhile to consider the overall spectral character that is observed. As with the phase spectra populations, we would argue that although the spectra are sorted into three population types in Table 2 for convenience, they are actually samples of the same population continuum. Instead of being the product of separate structuring mechanisms, they are manifestations of the same process encountered under different conditions. For both altitude periods, the average of the two-component spectral indices is nearly exactly the same as the measured single power-law index: this is

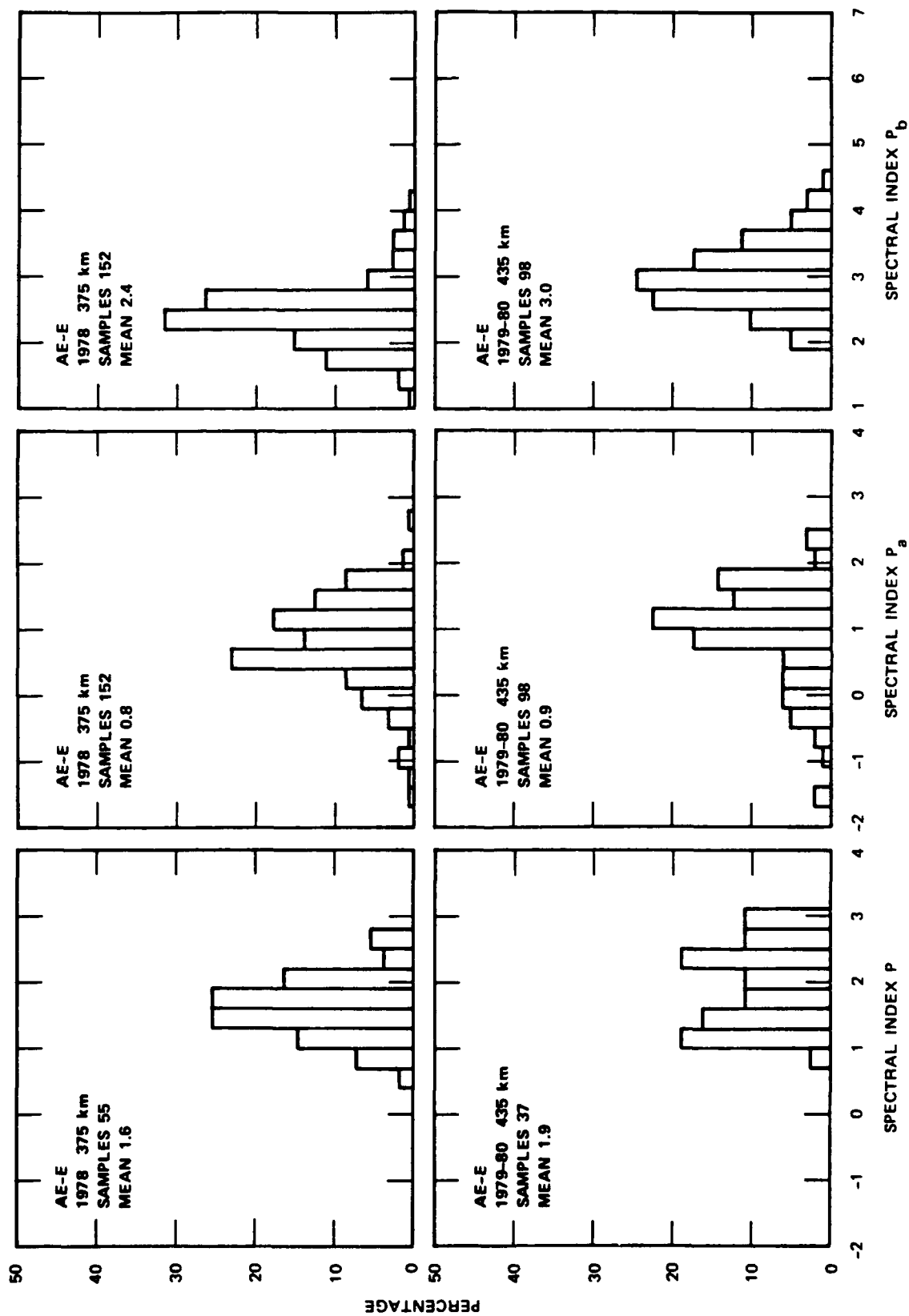


Figure 9. Distributions of Spectral Indices for Single Power-Law and Two-Component Spectral Forms.

because the average of the indices is a good approximation to what would be obtained using a single power-law fit over the entire spectrum. The same is true for the 375-km altitude, three-component indices.

There are few data with which to compare the slope information in Table 2, other than the phase data presented in Section 2. Examples of in situ irregularity spectra measured by AE-E are presented in a few papers (e.g., *McClure et al.*, 1977) but there have been no systematic studies of ionospheric irregularity spectra in the 200- to 2500-m spatial wavelength "freezing window." *Livingston et al.* (1981) present spectral results from low-resolution AE-E data, based upon single power-law fits made at longer wavelengths (750 to 7500-m). The physics controlling the spectral shape at those longer wavelengths appears to be quite different from that controlling the intermediate scale structure, and comparisons between these data and those of *Livingston et al.* (1981) are not appropriate.

The statistical summary of the irregularity spectral slopes in Table 2 shows that despite the similarity of background conditions and structuring levels, the two different year/altitude/- longitude sets show some differences. The 435-km single power-law slopes are considerably steeper than those at 375 km. The two-component slope values suggest that this difference arises from a steeper spectrum at short spatial wavelengths; there is very little difference between the slopes at wavelengths larger than the freezing scale.

It is difficult to determine any specific reason for these differences because of the separation of the data sets in solar cycle, longitude (through magnetic field configuration), and altitude. Any of these factors

can affect the growth and dissipation mechanisms that determine the details of the short-wavelength portion of the spectra.

The measured distributions of the two-component spectral break wavelength are shown in Figure 10, and are summarized in Table 2. For each spectrum in the two-component populations, the break wavelength data have been converted to an equivalent cross-field dimension, based upon the satellite orbit and the DGRF-75/80 magnetic field model. It is interesting to note from Figure 10 that the distribution of break scales is relatively uniform over the standard deviation range shown in Table 2.

Unlike the spectral slopes, which differ between the two different altitude sets, there is only a small difference between the average freezing break wavelengths at 375 and 435 km. The small change that is seen is attributable to the occurrence of more larger-scale ( $> 1100$  m) breaks in the 375-km data, as the distributions in Figure 10 illustrate.

Although the specific mechanisms for control of the freezing break are not completely understood, it is likely that collisionality plays a significant role. The neutral atmospheric density, and therefore the collision frequency, decreases exponentially with altitude. In the collision-dominated F region, the irregularity growth rate is inversely proportional to collision frequency; one would expect, to first order, that this would result in an altitude dependence of the freezing scale wavelength. It is therefore somewhat surprising to find such close agreement in break scales measured at 375 and 435 km. Accordingly, we have considered the collision conditions for the two data sets in more detail.

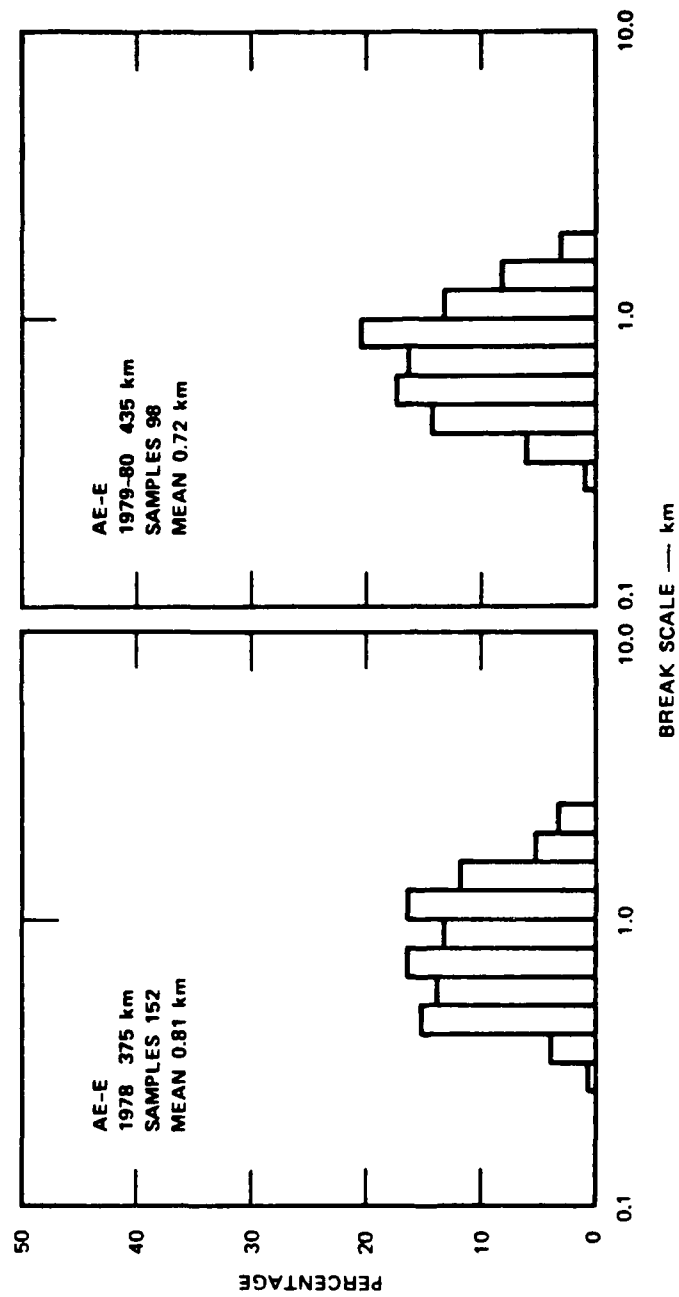


Figure 10. The Distributions of Spectral Break Wavelength Measured by the AE-E Satellite at Two Different Altitudes.

The average ion-neutral collision frequency for the two time periods of AE-E data has been estimated from measured F10.7 solar flux. *Kelly et al.* (1983) present the daily mean exospheric temperature versus solar flux for a solar cycle of Chatanika radar observations. A fit to their data gives the expression

$$T_{\infty} = 685. + 2.54 * F_{10.7}$$

For the AE-E data periods in 1978 and 1979-1980, the average estimated exospheric temperatures are 1041 K for the Pacific sector data and 1180 K for the Atlantic sector data. Figure 11 shows the altitude variations of the ion-neutral collision frequencies based on the Jaccia neutral density model and using the momentum transfer cross-section coefficients after *Schunk and Walker* (1973). As the figure shows, the intervening year of increasing solar flux reduces the collision frequency change between 375 and 435 km. However, even the change from 0.20 to 0.12 Hz should produce a measurable increase in the freezing break between the lower- and higher-altitude data periods; the data do not show such a change.

There are a number of reasons that this first-order application of collision control of the freezing break might not apply to the

AE-E data. The control of the freezing break may be much more complex than we have suggested, but there also may be a relatively simple explanation. The basic assumption used above is that the freezing break is set by a single, constant driver (gravity) under conditions in the irregularity locale. The PLUMEX rocket data that will be presented in Section 4 support this assumption, except that the freezing break in those data appear to be set by local conditions at the time and place that the irregularities were created. As is well known, the dynamics of growth-phase equatorial bubbles can rapidly transport kilometer-scale structure over a large altitude range. Furthermore, any dominant kilometer-scale structure should map along field lines. Thus, AE-E in an orbit that traverses approximately  $\pm 20$  degrees of dip latitude, will sample a complicated composite of freezing breaks that reflect a wide variety of irregularity generation conditions.

In contrast to this broad time and space coverage of AE-E, in the next section we review data from the PLUMEX II rocket. These data provide a means to obtain spectral shape under known local conditions and over a short enough period in time that any drivers are constant.



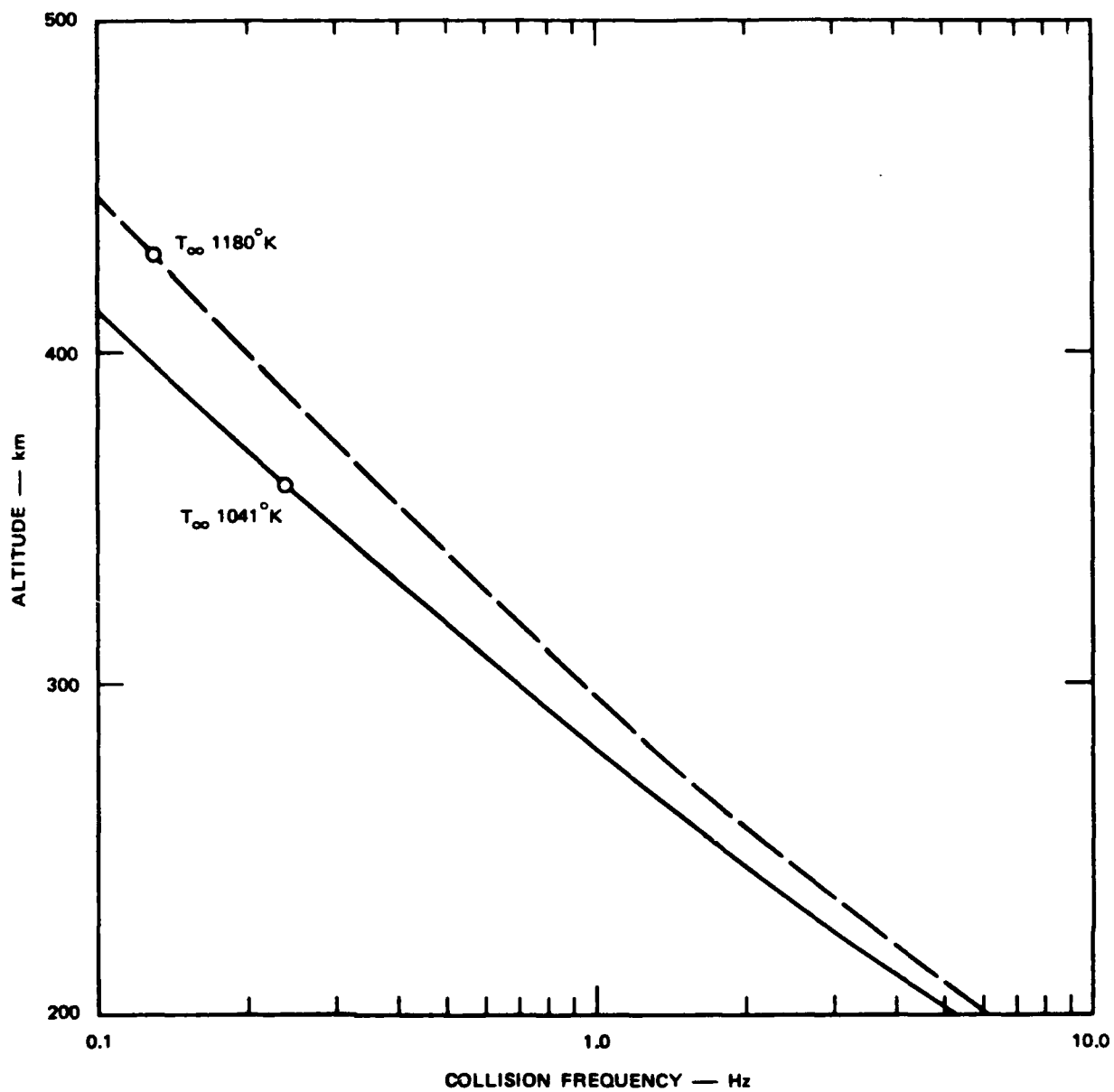


Figure 11. Collision Frequency Profiles Estimated on the Basis of the Measured F10.7 cm Flux and the Jacchia Neutral Atmosphere Model.

## SECTION 4

### PLUMEX DATA; VERTICAL, ONE-DIMENSIONAL SCANS

The DNA PLUMEX II rocket was launched in July 1979 from Kwajalein Atoll into fully developed, early decay phase ionospheric F-region structure. Its trajectory followed the central stem of an equatorial plume that extended from the bottomside through the topside of the F layer. During its upleg flight, the rocket passed through a highly structured F region and then a distinct topside depletion. On the downleg flight, the rocket again penetrated the depletion, at a slightly more northerly latitude, and encountered F-region structure similar to that seen on the upleg.

The PLUMEX data have been discussed in several papers and reports. Most notably, *Kelley et al.* (1982) studied short-scale structure, and *Rino et al.* (1981) considered intermediate-scale (100- to 2000-m) irregularities. *Rino et al.* (1981) performed spectral analysis on a broad-altitude segment of the F-layer electron density profile, and found a two-component power-law form, with a break near 800 m. This is very similar to the statistical characterization obtained from the AE-E data presented in Section 3. The implication of this agreement is that vertical and horizontal in situ scans (both cross field) are essentially equivalent, (i.e., there is little anisotropy in the plane perpendicular to the magnetic field) and that the PLUMEX data provide a representative view of the altitude dependencies of equatorial irregularity processes at intermediate scale sizes.

Because it was computed over such a large altitude range, the *Rino et al.* (1981) spectral result provided only a look at the

dominant irregularity structure in the F region. With the emergence of theories to explain multicomponent spectra, we have returned to the PLUMEX data to make a closer examination of the irregularity spectral forms that were observed. The PLUMEX experiment was unique in that it provided a means to examine altitude dependencies in the irregularity processes, a dimension not generally available from satellites. In particular, it is possible to determine the altitude dependence of the break point.

We first consider the overall geometry of the PLUMEX experiment, which has an important bearing on the upleg/downleg spectral comparisons. Figure 12 shows the rocket trajectory (solid curve) and magnetic field lines (DGRF75) at three altitudes, traced from the downleg to the upleg and on southward to the magnetic equator. The altitudes of the field lines at their intersections with the trajectory and the magnetic equator are noted. In actuality, the rocket trajectory was not in the magnetic meridian (8.5 degrees azimuth) as Figure 12 implies; instead it was launched at about 25 degrees azimuth, which allowed interception of the eastward drifting plume during both the upleg and downleg flights. Several features of the macroscale structure encountered during the upleg were also observed during the downleg.

Figure 13 shows the plasma density profiles obtained during the upleg and downleg. The topside bubble (at 475 km on the upleg) was encountered at about 440 km on the downleg; the same structured sublayer

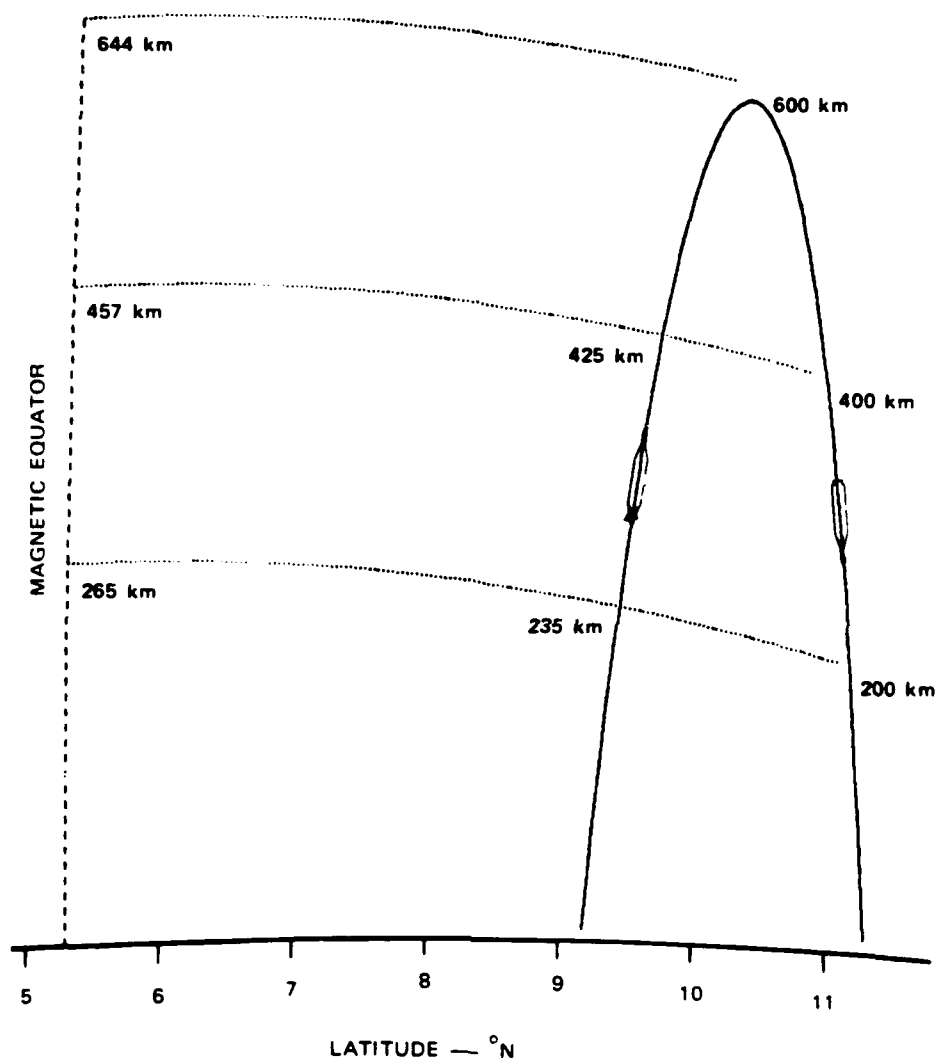


Figure 12. Geometry of the PLUMEX I Experiment. Showing the Rocket Trajectory and Magnetic Field. Altitudes of the field line intersections with the trajectory and the magnetic equator are as indicated.

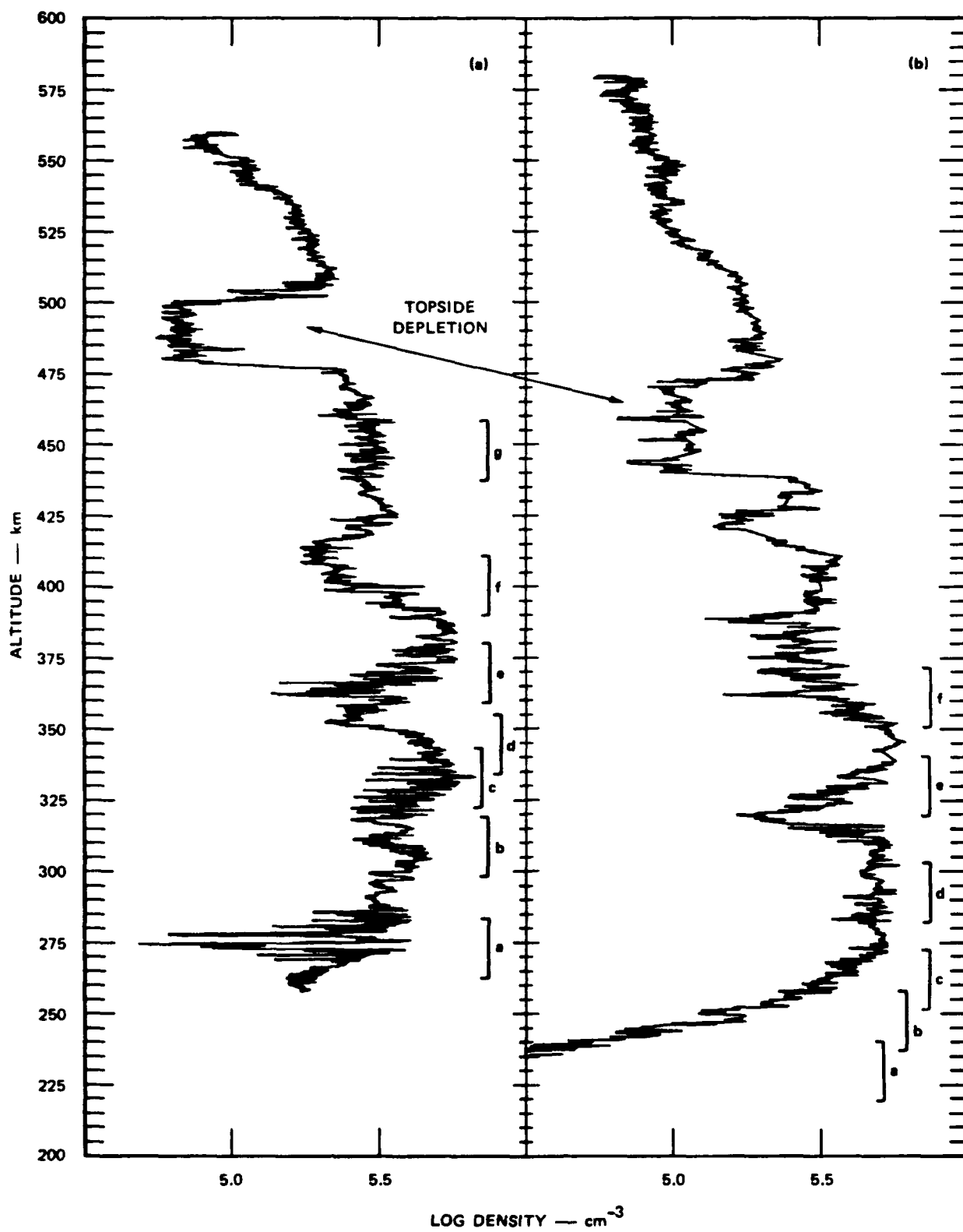


Figure 13. Plasma Density Profile Measured by the PLUMEX Rocket on the Uplog and Downleg Respectively.

seen between 355 and 410 km upleg, is seen between 320 and at 375 km on the downleg. The altitude differences between the upleg/downleg macroscale plasma features coincide well with the altitude variation of the magnetic field lines shown in Figure 12. The implication is that the macroscale plasma features in the middle and upper F layer map from upleg to downleg along the magnetic field. The profiles also suggest that local aeronomy, rather than mapping, controls the layer shape at low altitudes. Using ALTAIR incoherent-scatter radar measurements made during a scan in the magnetic meridian, *Tsunoda* (1980) showed similar field alignment of macroscale plasma structure at high altitudes, and the control of the bottomside F layer by recombination chemistry. In our case, this handoff between mapping and aeronomy processes occurs at an altitude of about 275 km. Similar conclusions were drawn by *Kelley et al.* (1986) in the CONDOR experiments.

The macroscale similarities between the upleg and downleg can be seen more conveniently in Figure 14, where the mean density and gradient scale are plotted versus altitude. Both parameters are computed over a 10-km interval in altitude. In the figure, the downleg data have been shifted upward in altitude by the amount determined by the field line trace, referencing them to the same magnetic altitude as the upleg.

Point by point, there are differences between the profiles, but the large-scale plasma sublayers and the gradient scales are quite similar, overall.

On the basis that the bulk plasma features map from the upleg to the downleg, one might expect that the intermediate-scale structure would also map. This does not

seem to be the case. Figure 15 shows that irregularity structure on the upleg is concentrated on the positive gradients of the profile; this would imply that the positive gradients were unstable to convective structuring prior to, or during, the upleg flight. In contrast, on the downleg profile there is no similar correlation between gradient sign and irregularity strength. Figure 15 specifically compares the altitude distribution of the intermediate-scale structure, after mapping the downleg statistics to the upleg altitude. The first parameter shown is the logarithm of the standard deviation in electron density,  $\sigma N$ . The second is the logarithm of the normalized deviation,  $\sigma N/N$ . Because we are concerned specifically with the structure in the freezing scale range, the parameters are obtained by integrating the spectral energy over a 2000- to 200-m wavelength window.

Because of the power-law nature of the irregularity spectrum, both parameters in Figure 15 are dominated by irregularities at the largest scales in this range, and these should effectively map along the magnetic field. However Figure 15 shows that the structure maxima do not correspond, indicating that the 1- to 2- km wavelength density irregularities do not map along the field from upleg to downleg. The most likely explanation is that the upleg and downleg trajectories penetrated slightly different parts of the plume—the upleg sampling the central stem, and the downleg sampling an edge where horizontal gradients could be important. An alternative, but probably less likely explanation in this case, is that irregularities with a real frequency component can transport themselves from the gradients on which they were produced (*Sperling and Glassman*, 1985). For our purposes here, however, the precise altitude distribution of irregularities

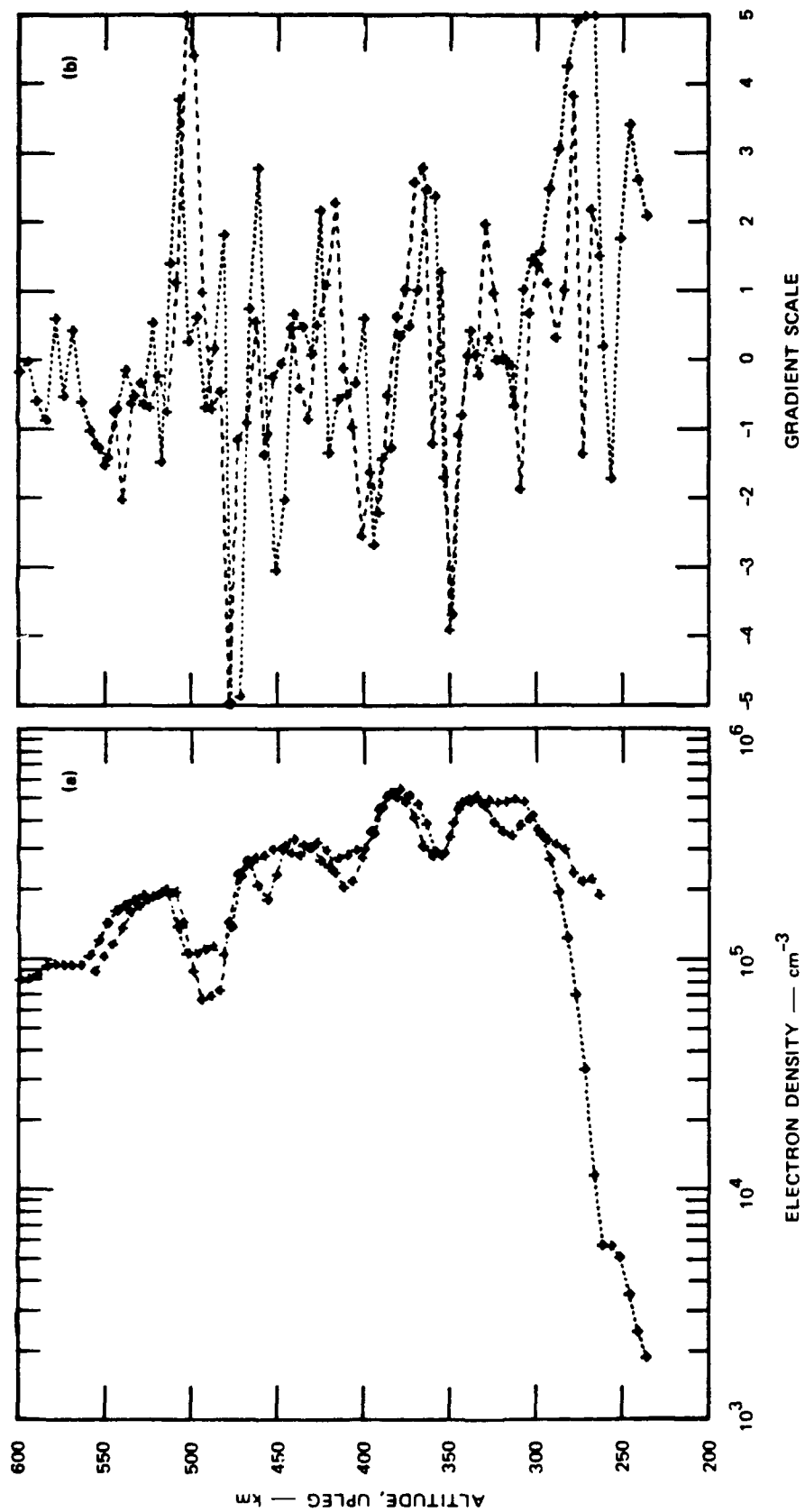


Figure 14. Macroscale Plasma Density Features Measured by the PLUMEX Rocket.

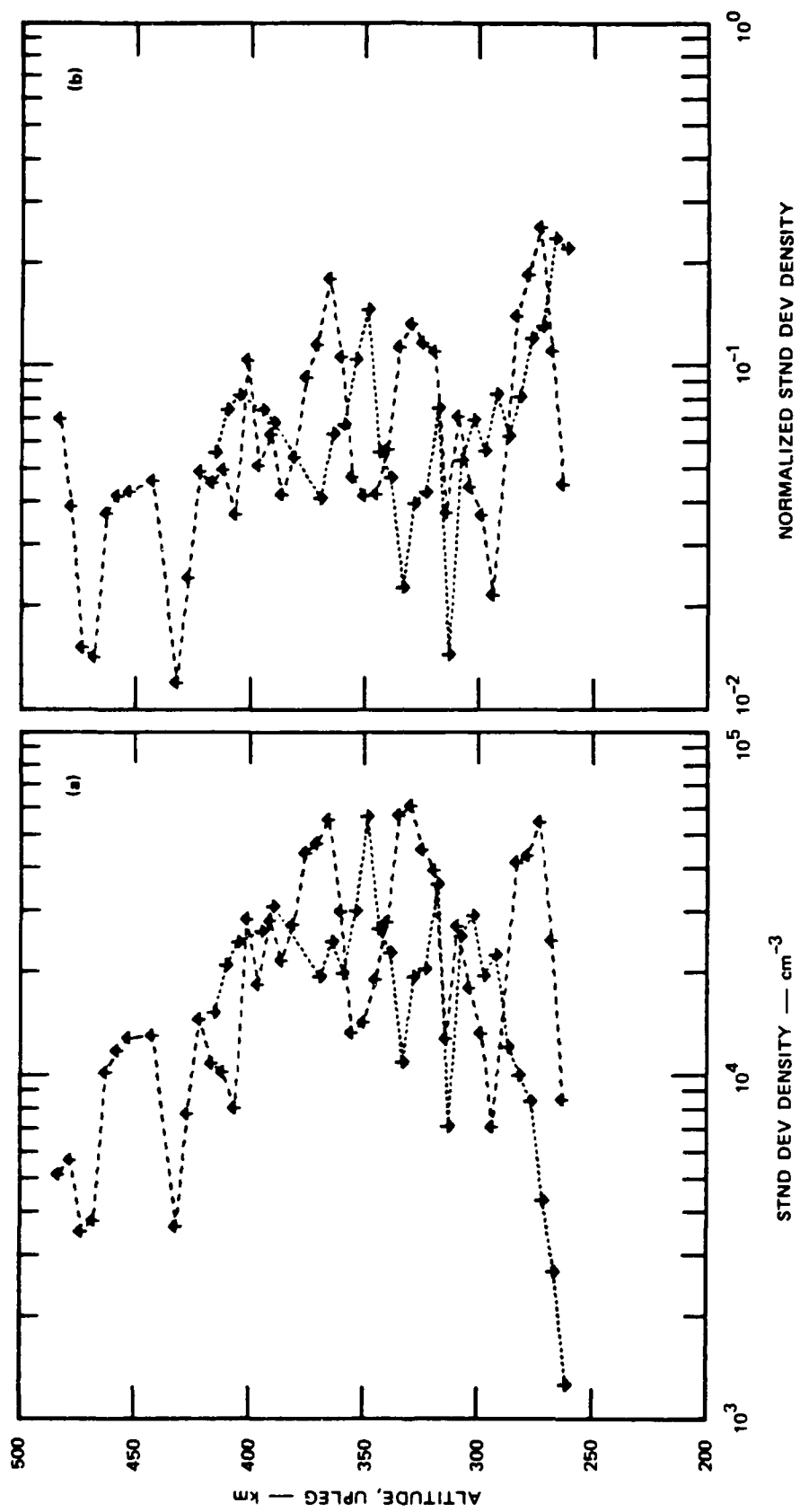


Figure 15. Plasma Irregularity Structure Measured by PLUMEX.

is less important than the fact that the perturbation levels of the upleg and downleg data are similar; this makes the direct comparison of their higher-order statistics more straightforward.

In this investigation, we have attempted to maximize the altitude resolution of the spectral analysis, in order to best observe height dependencies of the break scales. This is easy to implement, but the results can be difficult to interpret in terms of trends in spectral shape. The best resolution that is practical is about 10 km in altitude, which is the minimum span suitable for spectral analysis. At this resolution, however, there is significant variability of spectral form from sample to sample, even when the structuring process is clearly dependent on altitude. For the analysis here, we have tried to simplify the spectral shape interpretation by selecting a series of 20-km spans of data that: (1) appear to be stationary, and (2) are regions over which the irregularity generation process is likely to be consistent. For example the spans selected for the upleg are the positive and negative gradients of the sublayers, as noted in Figure 14. This selection of specific spans assures that if the break scale depends on either the driver or the disturbance level, the difference in break scale between those spans will not be obscured. Within each 20-km span, spectra are computed from 10-km, overlapped, altitude ranges (the top, bottom, and middle 10 km of the data). By using three individual spectra, we can convey some qualitative measure of the spectral variability (or consistency) which can occur over each narrow (20-km) altitude range.

Figure 16 shows data from one low-altitude portion of the upleg. Because spectral shape is our primary concern, the three individual (10-km overlapped) spectra are

averaged in log power to obtain the mean shape (for the overall 20-km span) shown as a dashed line. Note that the mean shape is not the same as the mean spectral density, which would follow the top of the envelope formed by the three curves. A fit is applied to the mean spectral shape in Figure 16 using the same interactive procedure as was used with the AE-E data. That is, break points are identified by eye, and slopes fits are made by the computer in a least-squares sense.

The spectra in Figure 16 are from the positive gradient region on the upleg F layer bottomside (260- to 310-km). All three altitude intervals are consistent in shape, both individually and on average, with a spectral break near 300-m wavelength.

Between the bottom and the top of the 20-km altitude span, there is a large difference in the fluctuation energy at long wavelengths, but at scales shorter than the break the slopes and energies are almost identical.

There are six other stationary data spans for the upleg flight (see Figure 13) in addition to that shown in Figure 16. The density data and spectra for four of these are shown in Figure 17. Both positive and negative gradient regions are represented among the segments; the clear differentiation between the amount of density structure suggests that these have been recently driven and nondriven, respectively. Also clear from Figure 17 is that there is a variation of the freezing break with altitude. Of the two other data spans not shown in the figure, one (segment b in Figure 13) is very similar in form to Figure 15. The other (segment g in Figure 13) is on the topside. It, too, shows a spectral break, but the spectral slopes are similar enough that the overall form can also be interpreted as single power law.



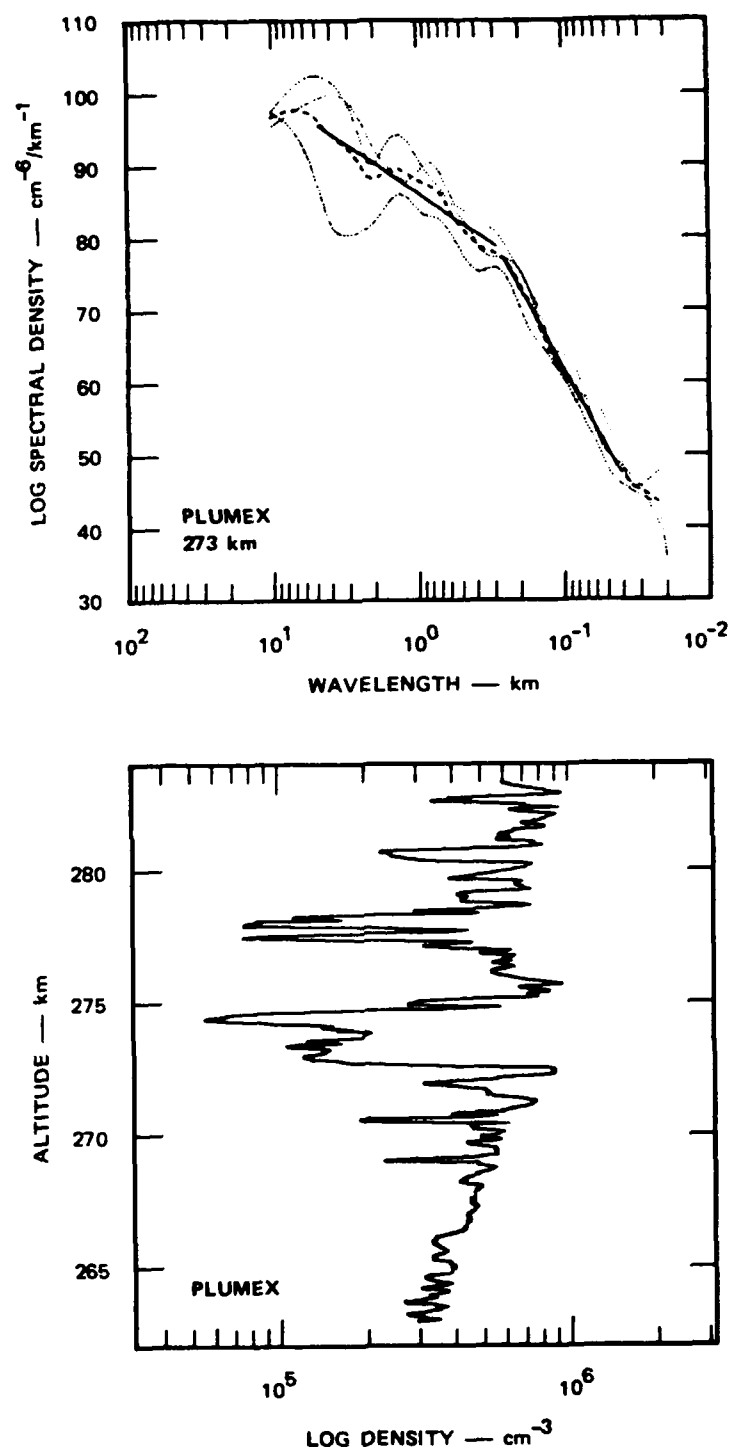


Figure 16. A 20 km Altitude Segment of the PLUMEX I Upleg Electron Density Profile and its Spectral Form. Shown are the spectra from three overlapped 10-km spectra (dotted), the average spectral shape (dashed), and the least squares fit to the average shape.

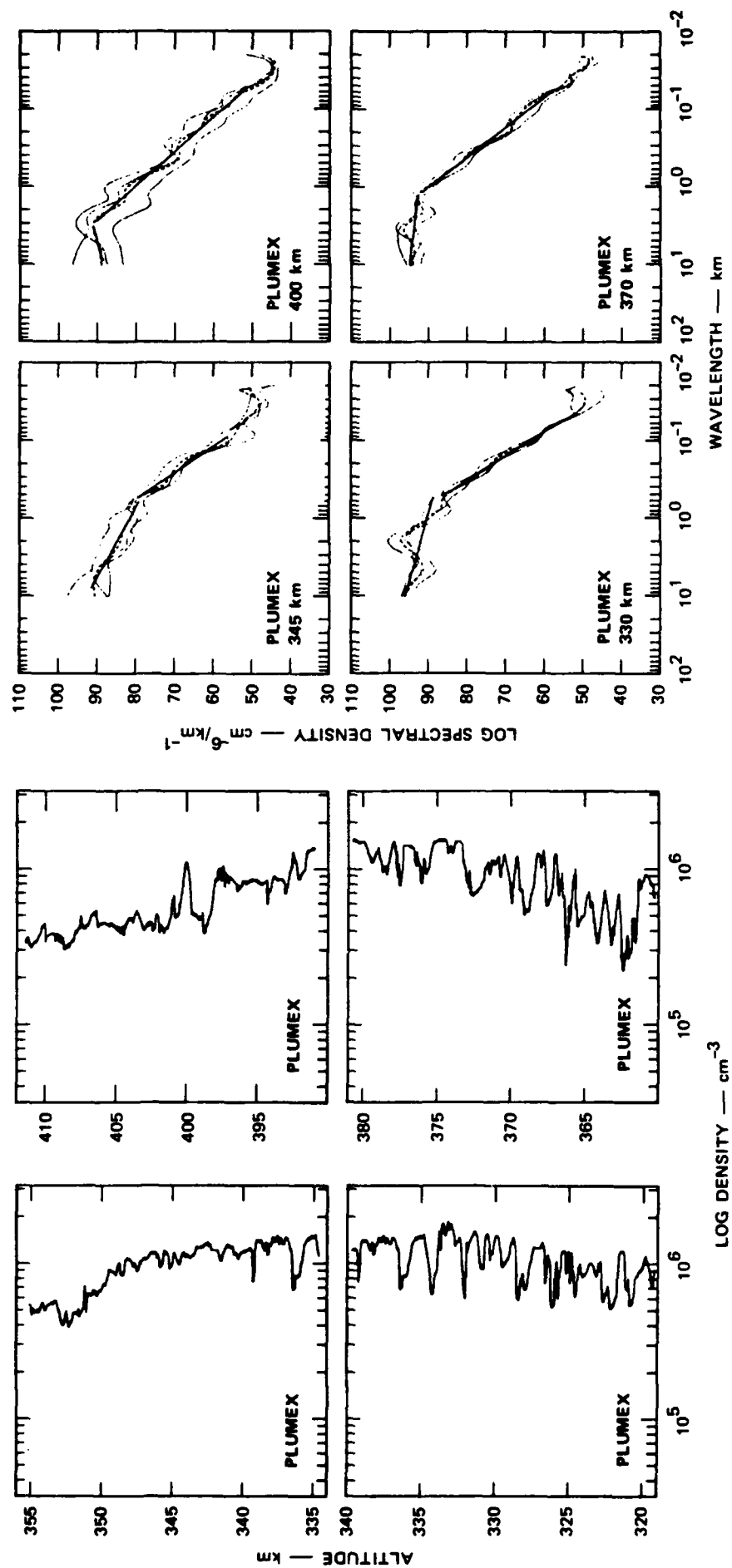


Figure 17. Plasma Irregularity Structure Measured by PLUMEX for Altitudes from 330 to 400 km.

Six segments of data from the downleg also have been analyzed. Telemetry data gaps limit these useful spans to altitudes below 380 km, as shown in Figure 13. As noted above, the macroscale features, but not the kilometer-scale structure, appear to map from the upleg to the downleg along the magnetic field. It can be safely assumed that the irregularity structures seen upleg and downleg were generated at approximately the same time, and through a similar process. The downleg structure is only slightly weaker in strength and is sampled about ten minutes after the upleg, so there should be little diffusive loss in spectral energy. In fact, this appears to be the case: the downleg spectra are similar to those in Figure 17 in terms of break wavelength variation and slope. The primary difference is that there is no ordering of the irregularity strength with gradient sign, as there is on the upleg.

The break wavelength data from all the upleg and downleg spectra are combined in Figure 18. The direction of the arrows at each point indicates which are from the upleg and which are from the downleg. In order to combine the data on a common vertical scale, we have used magnetic altitude—that is, the height at which the magnetic field line for each sample segment crosses the magnetic equator.

In effect, this simply means that the downleg samples are shifted upward about 30 km relative to the upleg samples, according to the magnetic field configuration in Figure 12. The shift is not essential to our conclusions, but brings the upleg and downleg samples into very close alignment. This alignment is the most obvious feature of Figure 18. There is a systematic ordering of all but the topside and bottomside break scales. They range from about 300 m at 270 km altitude, to larger than a kilometer at 400 km altitude.

There is also a change of spectral slope with altitude, as the spectra in Figures 16 and 17 imply. Overall, the indices of the two power-law components of the spectra both become more shallow with increasing altitude. The average slopes for the two-component spectra whose breaks lie along the main sequence in Figure 18 are  $p_a = 0.8$  and  $p_b = 3.3$ . The shallower slope is in good agreement with the horizontal scan AE-E value (Table 2): the dissipation regime slope is significantly steeper than the AE-E average. As mentioned above, the highest altitude spectrum is better characterized as single power law in form. This is also true for the next spectrum down in altitude, where the break wavelength approaches the large scale limit of the spectrum. For these topside samples, the spectral form approaches  $k^{-2}$ .

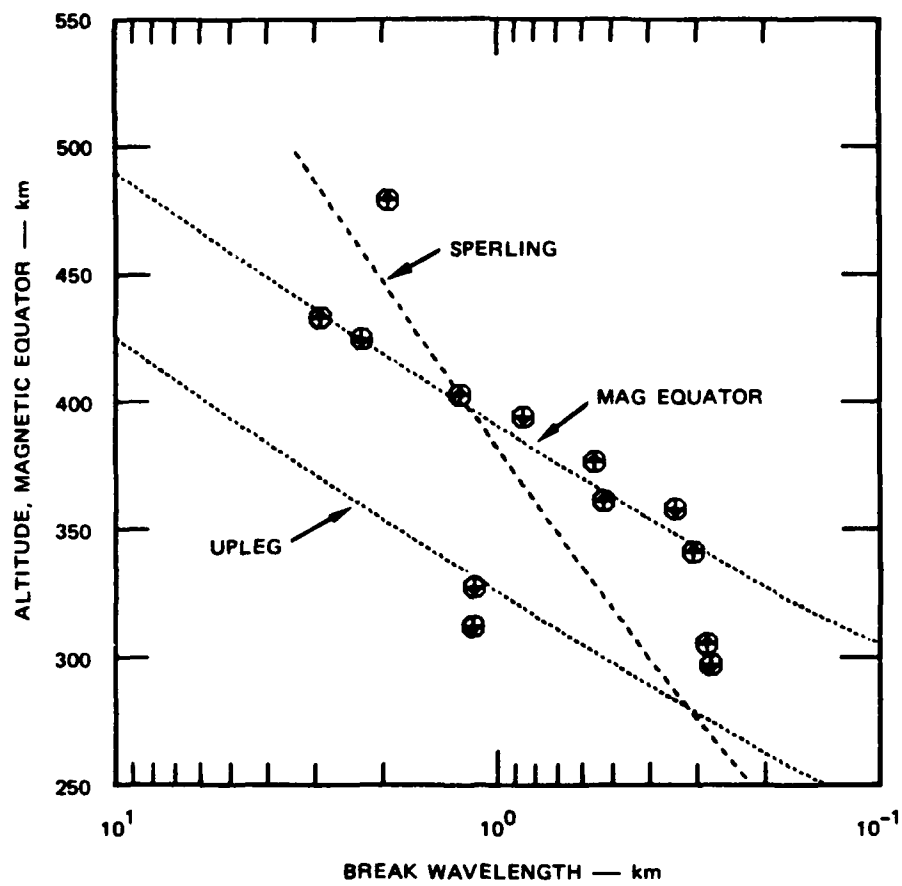


Figure 18. Altitude profile of break scales measured by PLUMEX.

## SECTION 5

### THE ALTITUDE DEPENDENCE OF THE FREEZING SCALE COMPARISON OF MEASUREMENTS WITH EXISTING THEORY

As was discussed in Section 4, to make the upleg and downleg PLUMEX data consistent in terms of a unique altitude dependence of the freezing scales, it was necessary to map the data to equal altitudes at the magnetic equator. This seems reasonable because that is where the driver is concentrated. We next wish to consider how the altitude dependence found compares with existing theoretical models.

One prominent model for the freezing scale, due to *Sperling and Glassman* (1985) has a relatively simple altitude dependence. In that theory, the freezing scale is controlled by a balance between growth and decay mechanisms, and has a  $v_{in}^{-1/2}$  dependence with altitude, where  $v_{in}$  is the ion-neutral collision frequency. The *Sperling and Glassman* (1985) prediction, for exospheric temperature of 800 K is superimposed in Figure 18. The agreement between observation and theory is reasonable, particularly at the lowest and highest altitudes. Overall, however, the slope of the prediction curve is too steep to match the bulk of the points. This suggests that a linear dependence on  $v_{in}^{-1}$  might provide a better fit to the break scale data, at least for the nonbottomside samples. This is, in fact, the case, as the curve (labeled magnetic equator) in Figure 18 illustrates. The linear growth rate is equal to  $\gamma = g_{eff}/v_{in}L$ , where  $g_{eff}$  is the effective gravitational constant and  $L$  is the gradient scale length. Using a simple dipole magnetic field model and taking into account the angle that the gravitational

vector makes with the field, it can be shown that  $g_{eff}$  is nearly constant along a given field line. The observed relationship between the break wavelength and  $v_{in}$  altitude profiles suggests a dependence of the break wavelength on  $\gamma_{eff} = g_{eff}/v_{in}$ , independent of the gradient scale.

To accept a  $v_{in}^{-1}$  dependence of the spectral break over the central portion of the F layer, some explanation is necessary as to why the bottomside spectral forms do not fit the same pattern. All of the spectra that deviate from the  $v_{in}$  curve at low altitudes occur below about 280 km true altitude and, we note from Figure 13, these segments are all on the F-layer bottomside. In terms of the overall data set, these points are different from those at higher altitudes: each is on a steep positive gradient and exhibits a large value of  $\delta N/N$ . This is illustrated more specifically in Figure 19, which is a scatter plot of gradient versus  $\sigma N/N$ , with the bottomside points circled. Both the steep gradient and the large  $\sigma N/N$  are indicators that, although the upper F layer may be stable, the bottomside may be actively structuring. If local conditions (rather than those at the magnetic equator) dominate, the theoretical curves in Figure 19 may move downward as much as 60 km in altitude. This local structuring  $v_{in}^{-1}$  dependence is also shown in Figure 19, and provides a reasonably good fit to the bottomside dependence we observe. This may be a fortuitous agreement, however, and it should be kept in mind that several

other factors could explain the difference in break wavelength behavior on the bottomside. Included among these is the

possibility of a vertical velocity shear (Tsunoda *et al.*, 1981), and the latitudinal dependence of the eastward neutral wind.

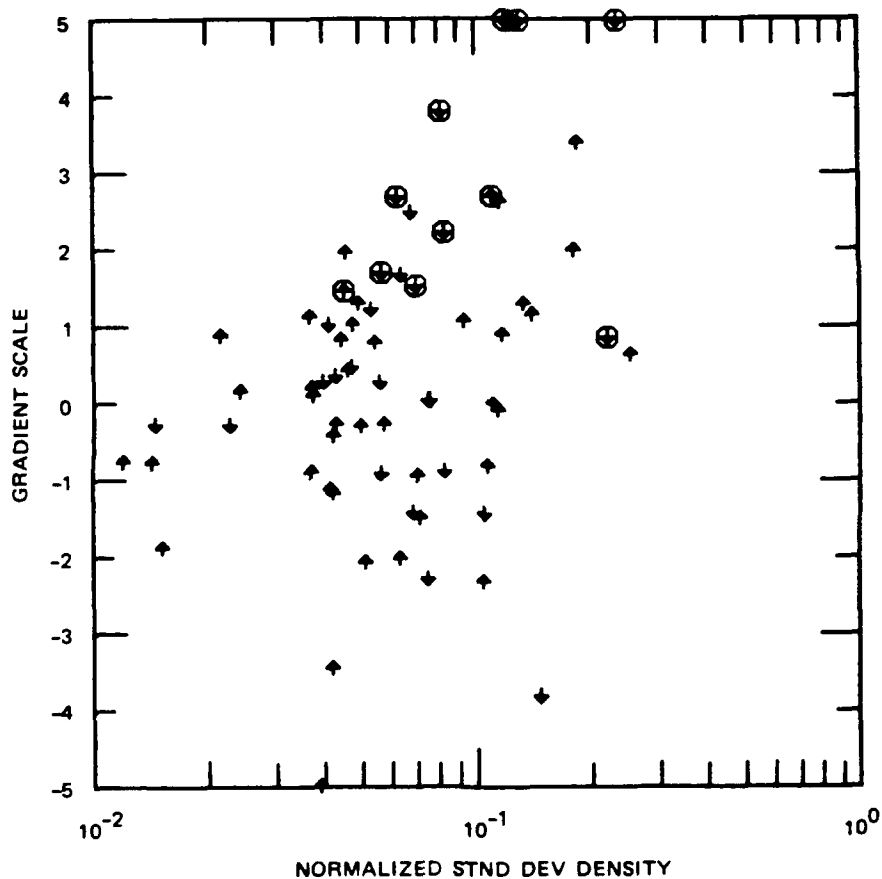


Figure 19. Scatter Plot of Gradient Scale versus  $\sigma N/N$  measured by PLUMEX.

## SECTION 6

### CONCLUSIONS

In this report, we have made a comprehensive experimental study of the spectral characteristics of equatorial ionospheric F-region structure. Included are the characterization of spectra measured using RF propagation, and in situ satellite and rocket observations scanning both vertically and horizontally across the magnetic field.

The vertical-scan PLUMEX rocket data are the easiest to interpret in terms of the physical processes that produce the irregularities. This is because the structuring processes appear to be consistent over the time and spatial extent of the measurement. Under those conditions, the irregularity power spectra on the topside of the F layer (i.e., inertia-dominated altitudes) are power law in form, with a one-dimensional slope  $p \sim 2$ . Lower in altitude (i.e., collision dominated), the spectra are two component in form, with a shallow intermediate scale regime and a more steeply sloped dissipation regime. The freezing scale, which we have associated with the break of slope in the two-component spectra, moves to larger scale sizes with increasing altitude. This altitude dependence is well matched by the inverse of the ion-neutral collision frequency. The comparison of the upleg and downleg data suggests that the freezing scale characteristics of an irregularity volume is determined by local conditions at the time and location of their origin.

The AE-E satellite data that have been analyzed were collected over a large spatial volume and over many hours of local time. Approximately one-third of those data are single power law in form, which is

consistent with the satellite altitude and the PLUMEX observations. Also consistent with the PLUMEX data is an average single power-law slope of  $p \sim 2$ . Among the dominant two-component population, there is no obvious collision dependence of the freezing break, even with changing satellite altitude. In light of the PLUMEX data and, in particular, the implication that the spectral shape is not necessary a reflection of local conditions, this is not surprising. On the other hand, the average PLUMEX vertical and AE-E horizontal spectral shapes are in good agreement; this suggests that spectral anisotropy, if present, is not major. The average break wavelengths of the vertical spectra are somewhat larger than the AE-E average, but are well within the statistical distribution observed by the satellite. The shallow intermediate slopes seen by AE-E and PLUMEX are essentially the same with a value  $p_a \sim 0.8$ . The dissipation regime average slopes from AE-E show a significant change with altitude, and are shallower than those seen by PLUMEX or implied from the phase scintillation data. The current analysis has not addressed this difference in detail, but subtle spectral anisotropy seems likely to be the cause. A value of  $p_b = 3.2$  can be used as an estimated average overall value of vertical/horizontal, one-dimensional slope in the dissipation regime.

Care must be taken to avoid strong scatter effects if phase scintillation data are to be used to imply the spectral form of in situ irregularities. In addition, a significant percentage of the phase spectra appear to be altered by superposition of energy from different altitudes. This is inherent in the

technique, but can be avoided by careful analysis. These disadvantages of the method are more than offset by its ease and economics as a morphological tool. The slopes of the single power-law phase data agree very well with the slopes observed in situ. The average value is near  $p = 3$ , which translates to a onedimensional slope of  $p = 2$ . This suggests that thin phase screen theory, which predicts this correspondence in weak scatter, is accurate. The two-

component phase spectral form is, on average, steeper than the in situ spectra in the intermediate-scale regime. The variation of this slope between station longitudes suggests that it is a result of leakage of superposed phase energy from structures much larger than a few kilometers. The dissipation regime slopes are, as noted above, in excellent agreement with those seen by PLUMEX, but steeper than the average in the AE-E statistics.



## SECTION 7

### LIST OF REFERENCES

- Chesnut, W.G., private communication.
- Fejer, B.G., and M.C. Kelley, "Ionospheric Irregularities," *Rev. Geophys. and Space Phys.*, 18, 401, 1980.
- Franke, S.J., and C.H. Liu, "Observations and Modeling of Multi-Frequency VHF and Gigahertz Scintillations in the Equatorial Region," *J. Geophys. Res.*, 88, 7075-7085, 1983.
- Fremouw, E.J., R.L. Leadabrand, R.C. Livingston, M.D. Cousins, C.L. Rino, B.C. Fair, and R.A. Long, "Early Results from the DNA Wideband Satellite Experiment—Complex-Signal Scintillation," *Radio Sci.*, 13, 167, 1978.
- Hanson, W.B., and R.A. Heelis, "Techniques for Measuring Bulk Gas-Motion from Satellites," *Space Sci. Instrumentation*, 493, 1975.
- Kelley, M.C., J. Labelle, E. Kudeki, B.G. Fejer, Sa Basu, Su Basu, K.D. Baker, C. Hanuise, P. Argo, R. Woodman, W. Swartz, D. Farley, and J. Meriwether, "The CONDOR Equatorial Spread F Campaign: Overview and Results of the Large-Scale Measurements," *J. Geophys. Res.*, 91, 5487, 1986.
- Kelley, M.C., R. Pfaff, K.D. Baker, J.C. Ulwick, R.C. Livingston, C.L. Rino and R.T. Tsunoda, "Simultaneous Rocket Probe and Radar Measurements of Equatorial Spread F - Transitional and Short Wavelength Results," *J. Geophys. Res.*, 87, 1575, 1982.
- Kelly, J.D., C.J. Heinselman, and J. Petriceks, "High Latitude Exospheric Temperatures Observed over a Solar Cycle," *Radio Sci.*, 18, 901, 1983.
- Livingston, R.C., "Comparison of Multifrequency Equatorial Scintillation: American and Pacific Sectors," *Radio Sci.*, 15, 801-814, 1980.
- Livingston, R.C., and T.M. Dabbs, "Phase Scintillation Under Weak and Strong Scatter Conditions," DNA Report DNA-TR-86-333, 1986.
- Livingston, R.C., C.L. Rino, J.P. McClure, and W.B. Hanson, "Spectral Characteristics of Medium-Scale Equatorial F-Region Irregularities," *J. Geophys. Res.*, 86, 2421-2428, 1981.
- McClure, J.P., W.B. Hanson, and J.F. Hoffman, "Plasma Bubbles and Irregularities in the Equatorial Ionosphere," *J. Geophys. Res.*, 82, 2650, 1977.
- Rino, C.L., private communication, 1986.
- Rino, C.L., and J. Owen, "Numerical Simulations of Intensity Scintillation Using the Power-Law Phase Screen Model," *Radio Sci.*, 19, 891-908, 1984.
- Rino, C.L., R.T. Tsunoda, J. Petriceks, R.C. Livingston, M.C. Kelley and K.D. Baker, "Simultaneous Rocket-Borne Beacon and In Situ Measurements of Equatorial Spread F - Intermediate Wavelength Results," *J. Geophys. Res.*, 86, 2411, 1981.
- Rino, C. L. "A Power Law Phase Screen Model for Ionospheric Scintillation 1. Weak Scatter," *Radio Sci.*, 14, 6, 1135-1145, 1979.
- Schunk, R.W., and J.C.G. Walker, "Theoretical Ion Densities in the Lower Atmosphere," *Planet. Space Sci.*, 21, 1875, 1973.

Sperling, J.L. and A.J. Glassman, "Short-Circuiting, Non-Viscous, and Non-Inertial Effects in Striation 'Freezing'," *J. Geophys. Res.*, 90, 8507, 1985.

Tsunoda, R.T., "Control of the Seasonal and Longitudinal Occurrence of Equatorial Scintillations by the Longitudinal Gradient in Integrated E Region Pedersen Conductivity," *J. Geophys. Res.*, 90, 447, 1985.

Tsunoda, R.T., and C.L. Rino, "A Comparative Analysis of Equatorial Spread

F and VHF Scintillation," DNA Report DNA-TR-81-106, 1982.

Tsunoda, R.T., R.C. Livingston and C.L. Rino, "Evidence of a Velocity Shear in Bulk Plasma Motion Associated with the Post-Sunset Rise of the Equatorial F Layer," *Geophys. Res. Lett.*, 8, 807, 1981.

Tsunoda, R.T., "Magnetic-Field-Aligned Characteristics of Plasma Bubbles in the Nighttime Equatorial Ionosphere," *J. Atmos. Terr. Phys.*, 42, 743, 1980.

## DISTRIBUTION LIST

DNA-TR-89-137

### DEPARTMENT OF DEFENSE

ASSISTANT TO THE SECRETARY OF DEFENSE  
ATOMIC ENERGY

ATTN: EXECUTIVE ASSISTANT

DEFENSE ADVANCED RSCH PROJ AGENCY

ATTN: CHIEF SCIENTIST

ATTN: GSD R ALEWINE

DEFENSE COMMUNICATIONS AGENCY

ATTN: DR P CROWLEY

ATTN: J DIETZ

DEFENSE INTELLIGENCE AGENCY

ATTN: RTS-2B

DEFENSE NUCLEAR AGENCY

ATTN: OPNA

ATTN: PRPD R YOHO

3 CYS ATTN: RAAE

ATTN: RAAE A CHESLEY

ATTN: RAAE A MARDIGUIAN

ATTN: RAAE D RIGGIN

ATTN: RAAE G ULLRICH

ATTN: RAAE K SCHWARTZ

ATTN: RAAE M CRAWFORD

ATTN: RAAE S BERGGREN

4 CYS ATTN: TITL

DEFENSE NUCLEAR AGENCY

ATTN: TDNM

2 CYS ATTN: TDTT W SUMMA

DEFENSE TECHNICAL INFORMATION CENTER

2 CYS ATTN: DTIC/FDAB

JOINT DATA SYSTEM SUPPORT CTR

ATTN: C-312

NATIONAL SECURITY AGENCY

ATTN: L PLUSWICK

STRATEGIC AND THEATER NUCLEAR FORCES

ATTN: DR E SEVIN

ATTN: DR SCHNEITER

ATTN: LC R DAWSON

STRATEGIC DEFENSE INITIATIVE ORGANIZATION

ATTN: EN

ATTN: EN LTC C JOHNSON

ATTN: PTN C GIESE

ATTN: PTP LTC SEIBERLING

ATTN: TN

STRATEGIC TARGET PLANNING

ATTN: JKC (ATTN: DNA REP)

ATTN: JKCS

ATTN: JLWT (THREAT ANALYSIS)

ATTN: JPEM

### DEPARTMENT OF THE ARMY

HARRY DIAMOND LABORATORIES

ATTN: SLCIS-IM-TL (TECH LIB)

INFORMATION SYSTEMS COMMAND

ATTN: STEWS-TE-N K CUMMINGS

U S ARMY ATMOSPHERIC SCIENCES LAB

ATTN: SLCAS-AE (DR NILES)

ATTN: SLCAS-AE-E

ATTN: SLCAS-AR DR H HOLT

U S ARMY FOREIGN SCIENCE & TECH CTR

ATTN: DRXST-SD

U S ARMY MISSILE COMMAND

ATTN: AIAMS-S/B J GAMBLE

U S ARMY MISSILE COMMAND/AMSMI-RD-CS-R

ATTN: AMSMI-RD-CS-R (DOCS)

U S ARMY NUCLEAR & CHEMICAL AGENCY

ATTN: MONA-NU

U S ARMY NUCLEAR EFFECTS LABORATORY

ATTN: ATAA-PL

U S ARMY STRATEGIC DEFENSE CMD

ATTN: CSSD-H-LS B CARRUTH

ATTN: CSSD-H-SA

ATTN: CSSD-H-SA/R SMITH

ATTN: CSSD-H-SAV

ATTN: CSSD-IN-T M POPE

U S ARMY STRATEGIC DEFENSE COMMAND

ATTN: ATC-O W DAVIES

ATTN: CSSD-GR-S W DICKINSON

USA SURVIVABILITY MANAGMENT OFFICE

ATTN: SLCSM-SE J BRAND

### DEPARTMENT OF THE NAVY

NAVAL ELECTRONICS ENGRG ACTVY, PACIFIC

ATTN: CODE 250 D OBRYHIM

NAVAL OCEAN SYSTEMS CENTER

ATTN: CODE 542, J FERGUSON

NAVAL RESEARCH LABORATORY

ATTN: CODE 2000 J BROWN

ATTN: CODE 2627 (TECH LIB)

2 CYS ATTN: CODE 4100 H GURSKY

ATTN: CODE 4121.8 H HECKATHORN

ATTN: CODE 4183

ATTN: CODE 4700 S OSSAKOW

ATTN: CODE 4701

ATTN: CODE 4720 J DAVIS

ATTN: CODE 4780 B RIPIN

ATTN: CODE 4780 DR P BERNHARDT

ATTN: CODE 4780 J HUBA

ATTN: CODE 5300

ATTN: CODE 5326 G A ANDREWS

ATTN: CODE 5340 E MOKOLE

ATTN: CODE 8344 M KAPLAN

NAVAL TECHNICAL INTELLIGENCE CTR

ATTN: DA44

**DNA-TR-89-137 (DL CONTINUED)**

NAVAL UNDERWATER SYSTEMS CENTER  
ATTN: CODE 3411, J KATAN

OFFICE OF CHIEF OF NAVAL OPERATIONS  
ATTN: OP 941D

OFFICE OF NAVAL RESEARCH  
ATTN: 1132SM/A TUCKER

SPACE & NAVAL WARFARE SYSTEMS CMD  
ATTN: PD 50TD  
ATTN: PD50TD1 G BRUNHART  
ATTN: PME 106-4 S KEARNEY  
ATTN: PME-106 F W DIEDERICH

THEATER NUCLEAR WARFARE PROGRAM OFC  
ATTN: PMS-42331F (D SMITH)

**DEPARTMENT OF THE AIR FORCE**

AFIA/INIS  
ATTN: AFIA/INKD MAJ SCHROCK

AIR FORCE CTR FOR STUDIES & ANALYSIS  
ATTN: AFCSA/SAMI  
ATTN: AFCSA/SASC

AIR FORCE GEOPHYSICS LABORATORY  
ATTN: J KLOUBACHAR  
ATTN: OP/W BLUMBERG  
ATTN: SANTI BASU  
ATTN: SUL

AIR FORCE OFFICE OF SCIENTIFIC RSCH  
ATTN: AFOSR/NP

AIR FORCE SPACE SYSTEMS DIVISION  
ATTN: YA  
2 CYS ATTN: YN

AIR FORCE TECHNICAL APPLICATIONS CTR  
ATTN: TN

AIR UNIVERSITY LIBRARY  
ATTN: AUL-LSE

STRATEGIC AIR COMMAND/XRFS  
ATTN: XRFS

WEAPONS LABORATORY  
ATTN: NTCA  
ATTN: WL/SUL

**DEPARTMENT OF ENERGY**

EG&G, INC  
ATTN: D WRIGHT

LAWRENCE LIVERMORE NATIONAL LAB  
ATTN: L-97 T DONICH

LOS ALAMOS NATIONAL LABORATORY  
ATTN: R W WHITAKER

SANDIA NATIONAL LABORATORIES  
ATTN: A D THORNBROUGH  
ATTN: CODE 9014 R BACKSTROM  
ATTN: D DAHLGREN  
ATTN: DIV 2344 ROBERT M AXLINE

ATTN: ORG 1231 J R LEE  
ATTN: ORG 9114 W D BROWN  
ATTN: TECH LIB

**OTHER GOVERNMENT**

CENTRAL INTELLIGENCE AGENCY  
ATTN: OSWR/NED  
ATTN: OSWR/SSD FOR L BERG

DEPARTMENT OF COMMERCE  
ATTN: G REEVE  
ATTN: J HOFFMEYER  
ATTN: W UTLAUT

U S DEPARTMENT OF STATE  
ATTN: PM/TMP

**DEPARTMENT OF DEFENSE CONTRACTORS**

AEROSPACE CORP  
ATTN: A MORSE  
ATTN: BRIAN PURCELL  
ATTN: C CREWS  
ATTN: C RICE  
ATTN: G LIGHT  
ATTN: I GARFUNKEL  
ATTN: J KLUCK  
ATTN: M ROLENZ

ATMOSPHERIC AND ENVIRONMENTAL RESEARCH INC  
ATTN: M KO

AUSTIN RESEARCH ASSOCIATES  
ATTN: J THOMPSON

BERKELEY RSCH ASSOCIATES, INC  
ATTN: C PRETTIE  
ATTN: J WORKMAN  
ATTN: N T GLADD  
ATTN: S BRECHT

CALIFORNIA RESEARCH & TECHNOLOGY, INC  
ATTN: M ROSENBLATT

CHARLES STARK DRAPER LAB, INC  
ATTN: A TETEWski

CORNELL UNIVERSITY  
ATTN: D FARLEY JR  
ATTN: M KELLY

DEFENSE GROUP, INC  
ATTN: M K GROVER

ELECTROSPACE SYSTEMS, INC  
ATTN: P PHILLIPS

EOS TECHNOLOGIES, INC  
ATTN: B GABBARD  
ATTN: R LELEVIER

GENERAL ELECTRIC CO  
ATTN: ROBERT H EDSALL

GENERAL RESEARCH CORP INC  
ATTN: J EOLL

GEO CENTERS, INC  
ATTN: E MARRAM

HARRIS CORPORATION  
ATTN: E KNICK

HSS, INC  
ATTN: D HANSEN

INFORMATION SCIENCE, INC  
ATTN: W DUDZIAK

INSTITUTE FOR DEFENSE ANALYSES  
ATTN: E BAUER

J S LEE ASSOCIATES INC  
ATTN: DR J LEE

JAYCOR  
ATTN: J SPERLING

JOHNS HOPKINS UNIVERSITY  
ATTN: C MENG

KAMAN SCIENCES CORP  
ATTN: DASAC  
ATTN: E CONRAD  
ATTN: G DITBERNER

KAMAN SCIENCES CORPORATION  
ATTN: B GAMBILL  
ATTN: DASAC  
ATTN: R RUTHERFORD

LOCKHEED MISSILES & SPACE CO, INC  
ATTN: J HENLEY  
ATTN: J KUMER  
ATTN: R SEARS

LOCKHEED MISSILES & SPACE CO, INC  
ATTN: D T RAMPTON

LTV AEROSPACE & DEFENSE COMPANY  
2 CYS ATTN: LIBRARY

M I T LINCOLN LAB  
ATTN: D TOWLE  
ATTN: M LEE

MARTIN MARIETTA DENVER AEROSPACE  
ATTN: J BENNETT

MAXIM TECHNOLOGIES, INC  
ATTN: J SCHLOBOHM

MCDONNELL DOUGLAS CORP  
ATTN: T CRANOR

MCDONNELL DOUGLAS CORP  
ATTN: J GROSSMAN  
ATTN: R HALPRIN

METATECH CORPORATION  
ATTN: R SCHAEFER  
ATTN: W RADASKY

METEOR COMMUNICATIONS CORP  
ATTN: R LEADER

## MISSION RESEARCH CORPORATION

ATTN: J KENNEALY  
ATTN: R ARMSTRONG  
ATTN: S DOWNER  
ATTN: W WHITE

## MISSION RESEARCH CORP

ATTN: B R MILNER  
ATTN: C LONGMIRE  
ATTN: D ARCHER  
ATTN: D KNEPP  
ATTN: D LANDMAN  
ATTN: DOCUMENT CONTROL/R BOGUSCH  
ATTN: F FAJEN  
ATTN: F GUIGLIANO  
ATTN: G MCCARTOR  
ATTN: K COSNER  
ATTN: M FIRESTONE  
ATTN: R BIGONI  
ATTN: R DANA  
ATTN: R HENDRICK  
ATTN: R KILB  
ATTN: S GUTSCHE  
ATTN: TECH LIBRARY

## MITRE CORPORATION

ATTN: DR M R DRESP

## MITRE CORPORATION

ATTN: R C PESCI  
ATTN: W FOSTER

NORTHWEST RESEARCH ASSOC, INC  
ATTN: E FREMOUW

PACIFIC-SIERRA RESEARCH CORP  
ATTN: H BRODE

PHOTOMETRICS, INC  
ATTN: I L KOFSKY

PHOTON RESEARCH ASSOCIATES  
ATTN: D BURWELL  
ATTN: O LEWIS

PHYSICAL RESEARCH INC  
ATTN: W SHIH

PHYSICAL RESEARCH INC  
ATTN: A CECERE

PHYSICAL RESEARCH INC  
ATTN: H FITZ  
ATTN: P LUNN  
ATTN: W HEUSER

PHYSICAL RESEARCH, INC  
ATTN: R DELIBERIS  
ATTN: T STEPHENS

PHYSICAL RESEARCH, INC  
ATTN: J DEVORE  
ATTN: J THOMPSON  
ATTN: W SCHLUETER

PHYSICS INTERNATIONAL CO  
ATTN: C GILMAN

**DNA-TR-89-137 (DL CONTINUED)**

R & D ASSOCIATES  
ATTN: F GILMORE  
ATTN: M GANTSWEG

R & D ASSOCIATES  
ATTN: J WALTON

RAND CORP  
ATTN: C CRAIN  
ATTN: E BEDROSIAN

RAND CORP  
ATTN: B BENNETT

RJO ENTERPRISES/POET FAC  
ATTN: STEVEN KRAMER  
ATTN: W BURNS

S-CUBED  
ATTN: C NEEDHAM  
ATTN: T CARNEY

SCIENCE APPLICATIONS INTL CORP  
ATTN: S ROSENCWEIG

SCIENCE APPLICATIONS INTL CORP  
ATTN: C SMITH  
ATTN: D HAMLIN  
ATTN: D SACHS  
ATTN: L LINSON

SCIENCE APPLICATIONS INTL CORP  
ATTN: J COCKAYNE

SCIENCE APPLICATIONS INTL CORP  
ATTN: H SUNKENBERG  
ATTN: LIBRARY

SRI INTERNATIONAL  
2 CYS ATTN: J F VICKREY  
2 CYS ATTN: R LIVINGSTON  
ATTN: R T TSUNODA  
ATTN: W CHESNUT  
ATTN: W JAYE

STEWART RADIANCE LABORATORY  
ATTN: R HUPPI

TELEDYNE BROWN ENGINEERING  
ATTN: J WOLFSBERGER, JR  
ATTN: N PASSINO

TOYON RESEARCH CORP  
ATTN: J ISE

TRW INC  
ATTN: DR D GRYBOS

TRW SPACE & DEFENSE SYSTEMS  
ATTN: D M LAYTON

USER SYSTEMS, INC  
ATTN: S W MCCANDLESS, JR

VISIDYNE, INC  
ATTN: J CARPENTER

**DIRECTORY OF OTHER**

BOSTON UNIVERSITY  
ATTN: MICHAEL MENDILLO